

New Preconditioners and Large-Scale Computations for Solving Problems in Cardiac Mechanics



Xiyao Li
New College
University of Oxford

A thesis submitted for the degree of
MSc in Mathematical Modelling and Scientific Computing

Trinity 2019

TO MY FAMILY.

Abstract

We propose and analyse the properties of a novel, robust, and efficient solver for a new class of models for the active deformation of cardiac tissue. The equations of hyperelasticity include the exact incompressibility constraint, an orthotropic exponential constitutive law, and an orthotropic active stress; and they are recast in terms of Kirchhoff stress, displacement, and pressure. We propose the augmented Lagrangian preconditioners and provide the numerical validation through a set of benchmark computational tests.

Contents

1	Introduction	1
2	Governing equations	3
2.1	Overview of cardiac physiology	3
2.2	Mathematical model	4
2.2.1	Finite-strain cardiac mechanics	5
2.2.2	Active stress model	7
2.2.3	Equations of motion	7
2.2.4	Activation and excitation-contraction coupling	9
2.3	Comparisons with mixed formulations from other studies	9
3	Numerical method	11
3.1	Weak formulation	11
3.2	Mixed Galerkin discretisation	12
3.3	Linearisation of the mechanical problem	13
3.4	Accuracy verification of the finite-dimensional approximation	15
4	Results without preconditioning	17
5	Preconditioning	22
5.1	Overview of preconditioning techniques	22
5.2	Schur complement reduction and the block preconditioner	23
5.3	The augmented Lagrangian preconditioner	23
5.4	Construction of the preconditioner in our particular setting	25
5.4.1	The field split method	25
5.4.2	The augmented term	26
5.4.3	The preconditioner	26
6	Results with preconditioning	28

7	Tests for the preconditioner	33
7.1	Test 1: deflection of a beam	33
7.2	Test 2: inflation of an ellipsoid	36
8	Conclusions and future work	40
8.1	Conclusions	40
8.2	Future work	40
	Bibliography	42

List of Figures

2.1.1 Front cut of heart [5]	3
2.2.1 Transmural configuration of muscle fibres, taken from [44]	6
4.0.1 Geometry and mesh for the ellipsoid, generated using Gmsh [31] . . .	17
4.0.2 Fibre directions on the ellipsoid	18
4.0.3 Contraction and inflation of the ellipsoid	19
4.0.4 The y-position of the apex	19
4.0.5 Wall-thickening of the ellipsoid	20
4.0.6 The displacement plot	20
6.0.1 Convergence plot for the positions of the epicardial apex at different values of γ , when $\zeta_{\text{stab}} = 50$	29
6.0.2 Convergence plot for the positions of the epicardial apex at different values of ζ_{stab} , when $\gamma = 10$	30
6.0.3 Mesh and fibre direction on a patient-specific left ventricular geometry	31
6.0.4 Contraction, twist, and inflation of the ventricle	31
6.0.5 Colour map of the displacement over different parts of the ventricle .	32
6.0.6 Wall-thickening effect of the ventricle	32
7.1.1 Mesh of geometry of the beam	33
7.1.2 Deflection of the beam	34
7.1.3 Convergence plot for z -deflection at the end point of the beam, for different values of ζ_{stab}	35
7.1.4 Convergence plot for z -deflection at the end point of the beam, for different values of γ	36
7.2.1 Geometry and mesh used for the inflation of the ellipsoid	36
7.2.2 Inflation of the ellipsoid.	37
7.2.3 Convergence plot for apex inflation, at different values of ζ_{stab}	38
7.2.4 Convergence plot for apex inflation, at different values of γ	39

List of Tables

3.4.1 Approximation errors for Kirchhoff stress, displacement, and pressure, associated with the mixed finite element method using different polynomial degrees $l \in \{0, 1\}$ for Holzapfel-Ogden material laws.	16
6.0.1 Average KSP per Newton iteration at different values of γ with $\zeta_{\text{stab}} = 50$, where KF denotes the convergence failure of the inner Krylov solve, and NF denotes the convergence failure of the outer Newton solve. . .	28
6.0.2 Average KSP per Newton iteration at different values of ζ_{stab} , with $\gamma = 10$	29
7.1.1 Average KSP per Newton iteration at different values of ζ_{stab} , where $\gamma = 10$	34
7.1.2 Average KSP per Newton iteration at different values of γ , with $\zeta_{\text{stab}} = 10$, where NF denotes the convergence failure of the outer Newton solve	35
7.2.1 Average KSP per Newton iteration at different values of ζ_{stab} , where $\gamma = 1$	37
7.2.2 Average KSP per Newton iteration at different values of γ , where $\zeta_{\text{stab}}=5$	38

Chapter 1

Introduction

Cardiac physiology has been studied extensively in the past few years. Main efforts were dedicated to understanding the complex, multi-scale, and multi-physics nature of the cardiac mechanics and its coupled electro-mechanical activities. However, there are still fundamental cardiac mechanisms that are not fully understood, for example, those related to cardiac arrhythmias, heart failure, and many other significant clinical problems. Medical researchers and mathematicians are thus driven to develop mathematical models that aim to describe and simulate the physiological and pathophysiological responses of the heart. As might be expected, the complexity arising from the physiological conditions of the heart translates into the complex structure of the model equations, solving for which requires the adoption of robust and efficient numerical methods.

The performance of the numerical solvers is particularly crucial to the clinical-based applications of the models developed in academic research. The primary difficulties not only lie with the high spatial and temporal resolutions required by the simulations of patient-specific physiological conditions, but also with the constrained time posed by clinical diagnosis. Within this context, the use of preconditioning techniques is mandatory for lowering the computational costs and improving the convergence of the numerical solvers. Compared to the increasing number of studies in developing models for cardiac mechanics, there are relatively few research concentrating on the efficient computations of the solutions for the model equations [23]. Land et al [38] proposed a modified Newton method and a strain prediction technique to reduce the number of Newton iterations needed, Sundnes et al [47] proposed an efficient linearization of coupled passive and active mechanics problems, Hadjicharalambous et al [33] presented a weakly penalized formulation for the problem to provide an efficient treatment of incompressibility, and Campos et al. proposed an augmented

Lagrangian preconditioner for the nearly incompressible cardiac mechanics adopting the Guccione constitutive formulations [32].

Based on the theoretical framework established by Propp last year [43], where a Holzapfel-Ogden constitutive model was adopted and the governing mechanical equations were recast into a three-field formulation expressed in terms of the Kirchhoff stress, the displacement, and the pressure. The goal of this dissertation project is to develop a novel, robust, and efficient augmented Lagrangian preconditioner for solving the large-scale problems arising from cardiac mechanics.

This dissertation is presented as follows. In Chapter 2, we derive the governing mechanical equations, with certain modifications compared to that of used by Propp in [43], in order to adapt to the construction of the preconditioner. In Chapter 3, we introduce the weak formulations, the mixed Galerkin discretisation, the linearisation of the mechanical equations, and in addition conduct a convergence test for the discretisation. In Chapter 4, we present numerical results obtained from solving the equations using direct solvers. We outline how the preconditioner is constructed in Chapter 5 and present numerical results as well as corresponding analysis in Chapter 6. The preconditioner is then validated through a set of benchmark computational tests proposed by Land et al. [37] in Chapter 7. Conclusions, along with possible future extensions of the project are discussed in Chapter 8.

The codes have been written in Python language with **Firedrake** (an automated system solving PDEs adopting the finite element method) [26] [45], and with **PETSc** (a library for sparse matrix computations) [16][17][18]. All tests have been implemented with MPI processes using 16 processors. The meshes have been generated using **Gmsh** [31] and the solutions have been visualised using **ParaView** [34].

Chapter 2

Governing equations

In this chapter we formulate the governing equations to be solved. Ingredients of the cardiac model which are key to the derivation of the equations will be introduced in Section 2.2, with their underlying physiological principles being summarised in Section 2.1.

2.1 Overview of cardiac physiology

We intend to provide a brief introduction to the principles behind a cardiac cycle. The goal is not to present comprehensive physiological analysis, but rather to highlight aspects that aid the model construction.

A simple illustration of the cardiac structure is shown in Figure 2.1.1 below by the front cut of a human heart. The heart is comprised of the left and right atria, together with the left and right ventricles.

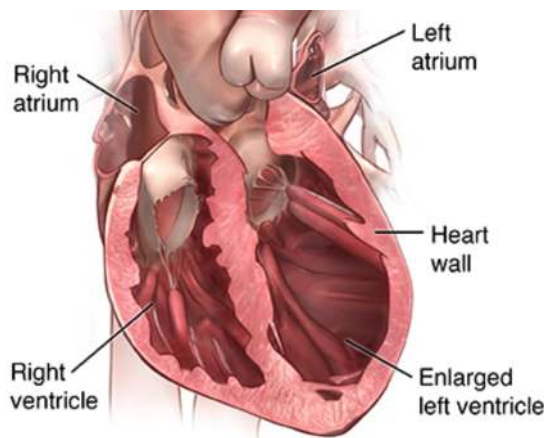


Figure 2.1.1: Front cut of heart [5]

The left ventricle is known to be under the highest blood pressure [2], since it is responsible for pumping oxygenated blood into the circulatory system, and therefore has become the main focus of most studies in the field of cardiology.

The blood filling of the ventricle is considered a passive process, and is a result of the cardiac suction which arises from the ventricular pressure difference [8]. On the other hand the ejection of blood from the ventricle into the circulatory system is an active process which is caused by the release of elastic strain energy. The accumulation of elastic strain is caused by the contraction of muscle fibres [41], which is in fact electrically-induced, its principles we shall introduce in the following paragraph.

The electrical current travelling through the heart arises from the movement of ions, which is triggered by a rapid rise or fall in the cardiac cell membrane potential (called human action potential) [9]. The inward current depolarizes and excites cardiac cells, whereas the outward current offsets the change in membrane potential through repolarisation. The aforementioned cardiac contraction (induced by fibre response) is a direct consequence of the repolarisation. The excitation-contraction coupling of this kind provides crucial link between the cardiac mechanics and electrophysiology.

The excitable cells constitute the cardiac tissue. The tissue is composed of three layers, namely the endocardium (inner tissue), the myocardium (core tissue), and the epicardium (outer tissue). The tissue is assumed to be orthotropic (materials that have three planes or axes of symmetry, with properties depending on the direction in which they are measured [11]), hyperelastic (materials with constitutive stress-strain relation derived from a strain energy density function [10]), and incompressible (materials with constant volume under deformation [6]).

2.2 Mathematical model

As mentioned in Chapter 1, our primary focus lies in developing a robust solver for the mechanical equations, since they possess the most complex and large-scale structure among the whole electromechanical coupling. Therefore to be more concise, we intentionally omit details of the electrical component of the model, and introduce in the following subsections only the parameters and concepts needed to define the mechanical component.

In order to adapt to the large deformations seen during the cardiac cycle, we describe the cardiac mechanics by theories of continuum mechanics, and the orthotropic constitutive relations by the Holzapfel-Ogden formulations [35].

2.2.1 Finite-strain cardiac mechanics

Let $\Omega \subset \mathbb{R}^d$ ($d \in \{2, 3\}$) be a deformable body in its reference configuration. The displacement field of an arbitrary material point \mathbf{x}_0 in Ω is denoted by

$$\mathbf{u} := \mathbf{u}(t, \mathbf{x}_0) : (0, t_{\text{final}}] \times \Omega \rightarrow \mathbb{R}^d,$$

and its new position \mathbf{x} in the deformed configuration is given by

$$\mathbf{x}(t, \mathbf{x}_0) = \mathbf{x}_0 + \mathbf{u}.$$

Here \mathbf{x} is also known as the deformation map, its gradient (with respect to fixed material coordinates) is given by the tensor

$$\mathbf{F} := \mathbf{I} + \nabla \mathbf{u}.$$

The solid volume change during the deformation, ρ_0/ρ (where ρ_0 and ρ denotes respectively the density of the undeformed and deformed material), is measured by the determinant $J = \det \mathbf{F}$. The incompressibility condition is incorporated as

$$J = \rho_0/\rho = 1. \quad (2.2.1)$$

We introduce the left Cauchy-Green deformation tensor $\mathbf{B} = \mathbf{F}\mathbf{F}^T$ and the right Cauchy-Green deformation tensor $\mathbf{C} = \mathbf{F}^T\mathbf{F}$. The first isotropic invariant of \mathbf{C} is defined by the scalar

$$I_1(\mathbf{C}) = \text{tr } \mathbf{C},$$

whereas its anisotropic pseudo-invariants are given by

$$I_{4,f}(\mathbf{C}) = \mathbf{f}_0 \cdot (\mathbf{C}\mathbf{f}_0), \quad I_{4,s}(\mathbf{C}) = \mathbf{s}_0 \cdot (\mathbf{C}\mathbf{s}_0), \quad I_{8,fs}(\mathbf{C}) = \mathbf{f}_0 \cdot (\mathbf{C}\mathbf{s}_0).$$

Here $\mathbf{f}_0, \mathbf{s}_0$ are generic unitary vectors pointing in the direction of cardiac fibres and the direction of the transversal sheetlet compound respectively, and $\mathbf{n}_0 = \mathbf{f}_0 \times \mathbf{s}_0$ is the unit normal in cross-fibre direction. The triplet $(\mathbf{f}_0(\mathbf{x}), \mathbf{s}_0(\mathbf{x}), \mathbf{n}_0(\mathbf{x}))$ is mutually orthogonal and thus can be seen as a coordinate system for the reference configuration. It is worth mentioning that the manner in which the heart can bend and twist is dictated by the orientation of the cardiac fibres [7]. Figure 2.2.1 below illustrates the transmural configuration of muscle fibres and laminar sheets, with the directions $\mathbf{f}_0, \mathbf{s}_0$ and \mathbf{n}_0 each being marked by arrows of different colours. Note that the coordinate system becomes $(\mathbf{f}_0(\mathbf{x}), \mathbf{s}_0(\mathbf{x}))$ when restricted to 2D.

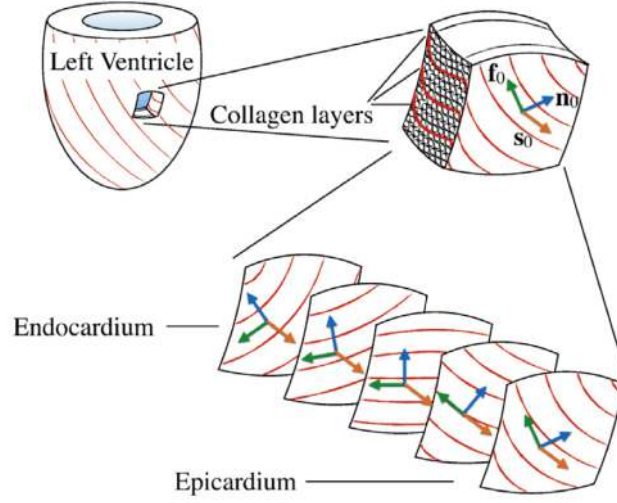


Figure 2.2.1: Transmural configuration of muscle fibres, taken from [44]

The constitutive relations of the myocardial tissue are described by the orthotropic model proposed by Holzapfel-Ogden in [35], where the strain energy density is given by

$$\Psi_{\text{pas}}(\mathbf{F}) = \frac{a}{2b} e^{b(I_1-d)} + \sum_{i \in \{f,s\}} \frac{a_i}{2b_i} [e^{b_i(I_{4,i}-1)_+^2} - 1] + \frac{a_{fs}}{2b_{fs}} [e^{b_{fs}(I_{8,fs})^2} - 1], \quad (2.2.2)$$

from which we can define the passive stress tensor:

$$\mathbf{P}_{\text{pas}} = \frac{\partial \Psi_{\text{pas}}}{\partial \mathbf{F}} - p \mathbf{J} \mathbf{F}^{-\text{T}}. \quad (2.2.3)$$

The passive stress is induced either by the left ventricular pressure or by the fibre stress. Here a, b are material constants associated with the isotropic matrix response, a_f and b_f describe the directional behaviour of the material along myocardial fibres, a_s and b_s describe the cross-contribution of the fibre sheet directions, and a_{fs}, b_{fs} describe the shear effects in the fibre-sheet plane [43]. The field p is the solid hydrostatic pressure, and $(\cdot)_+$ is the function defined by

$$(x)_+ = \begin{cases} x & x > 0, \\ 0 & \text{otherwise.} \end{cases}$$

The reason for taking only the positive part of the exponents is because we want to exclude anisotropic energetic contributions for compressed fibre configurations, since fibres tend to behave differently under compression and tension regimes [42].

2.2.2 Active stress model

Having defined the passive stress tensor, we assume that the first Piola-Kirchhoff stress tensor can be decomposed into a passive component and an active component, namely

$$\mathbf{P} = \mathbf{P}_{\text{pas}} + \mathbf{P}_{\text{act}}, \quad (2.2.4)$$

where the passive stress component was introduced earlier in equation (2.2.3) and the active stress component, based on the formulation proposed in Usyk et al. [48], takes the form

$$\mathbf{P}_{\text{act}} = J \boldsymbol{\sigma}_{\text{act}} \mathbf{F}^{-\text{T}}. \quad (2.2.5)$$

$\boldsymbol{\sigma}_{\text{act}}$ is known as the active Cauchy stress tensor,

$$\boldsymbol{\sigma}_{\text{act}} = \frac{T_a}{J\lambda_f} \mathbf{F} \mathbf{f}_0 \otimes \mathbf{F} \mathbf{f}_0 + \frac{\kappa_{sn} T_a}{J\lambda_s \lambda_n} \text{sym}(\mathbf{F} \mathbf{s}_0 \otimes \mathbf{F} \mathbf{n}_0) + \frac{\kappa_{nn} T_a}{J\lambda_n} \mathbf{F} \mathbf{n}_0 \otimes \mathbf{F} \mathbf{n}_0, \quad (2.2.6)$$

where T_a is the scalar field of active tension, κ_{sn} and κ_{nn} are positive constants representing the variation of activation in specific directions. λ_f , λ_s , and λ_n denote respectively the fibre stretch, sheetlet stretch, and cross-fibre stretch, with detailed expressions given by

$$\lambda_f = \sqrt{I_{4,f}}, \quad \lambda_s = \sqrt{I_{4,s}}, \quad \lambda_n = \sqrt{\mathbf{n}_0 \cdot (\mathbf{C} \mathbf{n}_0)}. \quad (2.2.7)$$

Active stress is responsible for additional deformation effects such as wall thickening, radial constriction and torsion, as well as longitudinal shortening without external load [48]. Note that the active Cauchy stress does not include the contribution from the diagonal entry associated with the local sheetlet direction \mathbf{s}_0 , since a stress component in this direction would counteract wall thickening mechanisms [27].

We remark that although there are plenty of cardiology studies incorporating the active stress formulation, (2.2.6) is the only model that produces physiologically relevant outcomes, such as wall-thickening and overall deformation. Other models where activation only occurs in the direction of fibres, generally lack most of the aforementioned physiological effects.

2.2.3 Equations of motion

From the conservation of linear momentum we can deduce

$$\rho \partial_{tt} \mathbf{u} - \nabla \cdot \mathbf{P} = \rho_0 \mathbf{b}, \quad \text{in } \Omega \times (0, t_{\text{final}}], \quad (2.2.8)$$

and the incompressibility constraint allows us to write

$$\rho J - \rho_0 = 0, \quad \text{in } \Omega \times (0, t_{\text{final}}]. \quad (2.2.9)$$

where \mathbf{b} is a smooth vector field of imposed body loads.

The Kirchhoff stress tensor $\mathbf{\Pi}$ is defined by

$$\mathbf{\Pi} = \mathbf{P}\mathbf{F}^T, \quad (2.2.10)$$

and is enforced to be symmetric in order to satisfy the conservation of angular momentum. An alternative way of writing the Kirchhoff stress tensor is to decompose it into the sum of two terms:

$$\mathbf{\Pi} = \mathcal{G} - p\mathbf{I}, \quad (2.2.11)$$

one being dependent on pressure, the other being pressure-free. Here \mathcal{G} is the pressure-free stress component, and

$$\mathcal{G} = \mathcal{G}(\mathbf{u}, T_a) := \frac{\partial \Psi}{\partial \mathbf{F}} \mathbf{F}^T + \mathbf{P}_{\text{act}} \mathbf{F}^T, \quad (2.2.12)$$

To summarise, the key ingredients of the mechanical model consist of the exact incompressibility constraint (equation (2.2.1)), an orthotropic exponential constitutive law (equation (2.2.2)), and an orthotropic active stress (equation (2.2.5)). These equations are recast in terms of Kirchhoff stress, displacement, and pressure, giving rise to the governing mechanical equations (2.2.8)-(2.2.9)-(2.2.11).

Adopting such three-field formulation is advantageous since the method itself can approximate the variables of interest, $(\mathbf{\Pi}, \mathbf{u}, p)$, directly, and provide robust solutions with balanced convergence order [43] in the incompressible regime.

We remark that the dominating feature to capture, and also the main difficulty to overcome when computationally solving the mechanical equations is the non-linearity in the Kirchhoff stress tensor $\mathbf{\Pi}$. It is justified in [25] that the time derivative has so little effect on the structure of the three-field formulation that we are actually able to neglect it, and consider only the stationary regime, where $\partial_{tt}u = 0$. Therefore equation (2.2.8) becomes

$$-\nabla \cdot \mathbf{P} = \rho_0 \mathbf{b}, \quad \text{in } \Omega \times (0, t_{\text{final}}]. \quad (2.2.13)$$

Suppose the domain Ω has a piecewise smooth boundary $\partial\Omega$ and let \mathbf{n} denote the outward unit normal vector on $\partial\Omega$. The governing equations are accompanied by boundary conditions

$$\mathbf{u} = \mathbf{0} \quad \text{on } \partial\Omega_D \times (0, t_{\text{final}}], \quad (2.2.14a)$$

$$\mathbf{\Pi}\mathbf{F}^{-\text{T}}\mathbf{n} - p_N J \mathbf{F}^{-\text{T}}\mathbf{n} = \mathbf{0} \quad \text{on } \partial\Omega_N \times (0, t_{\text{final}}], \quad (2.2.14b)$$

$$\mathbf{\Pi}\mathbf{F}^{-\text{T}}\mathbf{n} + \eta J \mathbf{F}^{-\text{T}}\mathbf{u} = \mathbf{0} \quad \text{on } \partial\Omega_R \times (0, t_{\text{final}}], \quad (2.2.14c)$$

where $\partial\Omega_D$, $\partial\Omega_N$, and $\partial\Omega_R$ together conform a disjoint partition of the boundary. The Dirichlet condition (2.2.14a) asserts that the motion along $\partial\Omega_D$ is constrained to be zero, the pressure condition (2.2.14b) states that the traction $\mathbf{t} = \mathbf{\Pi}\mathbf{F}^{-\text{T}}\mathbf{n}$ balances out the contribution made by p_N (a prescribed boundary pressure) when applied to the epicardium in the normal direction, and the Robin condition (2.2.14c) accounts for stiff springs connecting the cardiac medium with the surrounding soft tissue and organs [43].

2.2.4 Activation and excitation-contraction coupling

As mentioned previously in the active stress formulation, the dependence of active mechanical deformation on excitation-contraction coupling is encoded through T_a , the active tension in the cells. So here we provide a simple description of how the active tension is produced.

The generation of T_a arises from the movements of ionic quantities (thus giving rise to change in calcium concentration) and the stretches of local fibres. Note that in the setting of this model, only linear dependence on the proxy of calcium concentration and local stretches are required in order to qualitatively capture the dynamics of active tension [43]. Such dependence however, relies on the coupling with the model of electrophysiology.

Since our primary focus does not lie in solving for the electro-mechanical coupling, it is sufficient for us to specify T_a as a preset expression that depends only on time. The expression will be defined in each example.

2.3 Comparisons with mixed formulations from other studies

Certainly there are other studies which have considered stress and strain in their models of constitutive relations, for example in [46] and [30]. However, instead of the Holzapfel-Ogden formulation, Ruiz-Baier [46] conducted analysis for the Neo-Hookean strain energy function, with the three-field formulation recast into $(\tilde{\sigma}-\mathbf{u}-p)$ (the first-Piola Kirchhoff stress tensor, the displacement, and the hydrostatic pressure), and the coupling was of a elasticity-reaction-diffusion type. Garcia-Blanco et al. [30], on the other hand, adopted the Holzapfel-Ogden formulation, but the three-field formulation was recast in terms of $(\mathbf{x}-\phi-p)$, in other words, the deformed position vector, the transmembrane potential, and the pressure.

So the $(\mathbf{\Pi}-\mathbf{u}-p)$ three-field formulation adopted by Propp [43] and this study is novel compared to other known formulations describing the active contraction of the heart. Recasting the formulation in this particular set of variables is advantageous, since solving for the Kirchhoff stress tensor simplifies the computation in a sense that it is symmetric [24], and participates actively in the electro-mechanical coupling.

Chapter 3

Numerical method

As outlined in Chapter 2, we have derived a three-field formulation that states the governing equations in terms of stress-displacement-pressure. In this chapter, we present the discretisation and linearisation of the mechanical equations.

3.1 Weak formulation

Given the three governing equations (2.2.13)-(2.2.9)-(2.2.11) and boundary conditions (2.2.14a)-(2.2.14b)-(2.2.14c), we briefly outline how the weak formulations are established.

Multiplying both sides of the equations (2.2.11)-(2.2.13)-(2.2.9) with their corresponding test functions $(\boldsymbol{\tau}, \mathbf{v}, q)$, integrating by parts over the domain Ω , and making use of relation (2.2.10) together with boundary conditions (2.2.14b) and (2.2.14c), we arrive at the following formulations:

$$\begin{aligned} \int_{\Omega} [\boldsymbol{\Pi} - \mathcal{G} + pJ \mathbf{I}] : \boldsymbol{\tau} &= \mathbf{0} \quad \forall \boldsymbol{\tau} \in \mathbb{L}_{\text{sym}}^2(\Omega), \\ \int_{\Omega} \boldsymbol{\Pi} : \nabla \mathbf{v} \mathbf{F}^{-\text{T}} - \int_{\partial\Omega_N} p_N J \mathbf{F}^{-\text{T}} \mathbf{n} \cdot \mathbf{v} + \int_{\partial\Omega_R} \eta J \mathbf{F}^{-\text{T}} \mathbf{u} \cdot \mathbf{v} &= 0 \quad \forall \mathbf{v} \in \mathbf{H}_0^1(\Omega), \\ \int_{\Omega} [J - 1] q &= 0 \quad \forall q \in L^2(\Omega), \end{aligned}$$

where we have taken $\boldsymbol{\Pi} \in \mathbb{L}_{\text{sym}}^2(\Omega)$ (the space of matrix-valued square integrable functions, with the symmetry arising from the conservation of angular momentum), $\mathbf{u} \in \mathbf{W}_0^{1,4}(\Omega)$ ($\mathbf{W}_0^{1,4}(\Omega) = \{\mathbf{u} : \mathbf{u} \in \mathbf{L}^4(\Omega), \nabla \mathbf{u} \in \mathbf{L}^4(\Omega), \text{ and } \mathbf{u} = \mathbf{0} \text{ on } \partial\Omega_D\}$ [12]) and $p \in L^2(\Omega)$ in order to successfully apply the Green's formula of integration. The choice of test function spaces for $(\boldsymbol{\tau}, \mathbf{v}, q)$ then follows from this assertion, namely $\boldsymbol{\tau} \in \mathbb{L}_{\text{sym}}^2(\Omega)$, $\mathbf{v} \in \mathbf{H}_0^1(\Omega)$ ($\mathbf{H}_0^1(\Omega) = \{\mathbf{u} \in \mathbf{H}_0^1(\Omega) : \mathbf{u} = \mathbf{0} \text{ on } \partial\Omega_D\}$) and $q \in L^2(\Omega)$. Moreover we remark that $\mathbf{b} = \mathbf{0}$ under the assumption of zero body loads, $J = 1$ under

the full incompressibility condition, and the colon operator “:” denotes the Frobenius inner product, which takes the component-wise inner product of two matrices.

3.2 Mixed Galerkin discretisation

The spatial discretisation follows the mixed Galerkin approach.

Let us denote by \mathcal{T}_h a regular partition of Ω into simplicial elements K of maximum diameter h_K , for example pair-wise disjoint triangles in 2D or tetrahedra in 3D, and define the mesh size by

$$h := \max\{h_K : K \in \mathcal{T}_h\}.$$

Let \mathcal{E}_h be the set of interior facets of the mesh, the jump of a quantity across a given facet $e \in \mathcal{E}_h$ is denoted by $[\![\cdot]\!]_e$.

The finite element scheme being used here, in its lowest order case, approximates entries of the symmetric Kirchhoff stress tensor by piecewise constants, the displacement by piecewise linear functions, and the pressure by piecewise constants.

Following from the above approximation choice, we introduce finite dimensional spaces \mathbb{H}_h (subset of $\mathbb{L}_{\text{sym}}^2(\Omega)$), \mathbf{V}_h (subset of $\mathbf{H}_0^1(\Omega)$), and Q_h (subset of $L^2(\Omega)$), each being defined for the generic order of approximation $l \geq 0$:

$$\begin{aligned}\mathbb{H}_h &:= \{\boldsymbol{\tau}_h \in \mathbb{L}_{\text{sym}}^2(\Omega) : \boldsymbol{\tau}_h|_K \in \mathbb{P}_l(K)^{d \times d}, \forall K \in \mathcal{T}_h\}, \\ \mathbf{V}_h &:= \{\mathbf{v}_h \in \mathbf{H}^1(\Omega) : \mathbf{v}_h|_K \in \mathbb{P}_{l+1}(K)^d, \forall K \in \mathcal{T}_h, \mathbf{v}_h = 0 \text{ on } \partial\Omega_D\}, \\ Q_h &:= \{q_h \in L^2(\Omega) : q_h|_K \in \mathbb{P}_l(K), \forall K \in \mathcal{T}_h\}.\end{aligned}$$

Here $\mathbb{P}_l(K)$ denotes the space of polynomial functions of degree $s \leq l$ defined locally on the element K .

The finite-dimensional weak formulation then becomes:

find $(\boldsymbol{\Pi}_h, \mathbf{u}_h, p_h) \in (\mathbb{H}_h, \mathbf{V}_h, Q_h)$ such that

$$\begin{aligned}\int_{\Omega} [\boldsymbol{\Pi}_h - \mathcal{G}(\mathbf{u}_h) + p_h J(\mathbf{u}_h) \mathbf{I}] : \boldsymbol{\tau}_h &= 0 \quad \forall \boldsymbol{\tau}_h \in \mathbb{H}_h, \\ \int_{\Omega} \boldsymbol{\Pi}_h : \nabla \mathbf{v}_h \mathbf{F}^{-\text{T}}(\mathbf{u}_h) - \int_{\partial\Omega_N} p_N \mathbf{F}^{-\text{T}}(\mathbf{u}_h) \mathbf{n} \cdot \mathbf{v}_h + \int_{\partial\Omega_R} \eta J \mathbf{F}^{-\text{T}} \mathbf{u}_h \cdot \mathbf{v}_h &= 0 \quad \forall \mathbf{v}_h \in \mathbf{V}_h, \\ \int_{\Omega} [J(\mathbf{u}_h) - 1] q_h + \sum_{e \in \mathcal{E}_h} \int_e \frac{\zeta_{\text{stab}}}{h_e} [p_h]_e [q_h]_e &= 0 \quad \forall q_h \in Q_h.\end{aligned}\tag{3.2.1}$$

Note that in order to enforce the solvability of the discrete problem, we have incorporated a stabilisation term at the end of the third equation in (3.2.1). This modification technique is the so-called pressure stabilisation method, treatments of similar kind can be found in literature [40] and [22]. ζ_{stab} here is a positive pressure stabilisation parameter. The stabilisation is achieved by adding a bilinear jump term to the weak formulation, which effectively penalises a jump in pressure between adjacent cells, thus minimizing the appearance of spurious oscillations in the solution. Notice that the boundary condition (2.2.14a) is incorporated as an essential condition on the displacement space.

3.3 Linearisation of the mechanical problem

The finite-dimensional nonlinear weak formulations (3.2.1) are then linearised following the Newton-Raphson approach. The problem now becomes:

Starting from a initial guess

$$(\mathbf{\Pi}_h^{k=0}, \mathbf{u}_h^{k=0}, p_h^{k=0}) = (\mathbf{\Pi}_h^n, \mathbf{u}_h^n, p_h^n),$$

find stress, displacement and pressure increments $(\delta \mathbf{\Pi}_h^{k+1}, \delta \mathbf{u}_h^{k+1}, \delta p_h^{k+1})$ for each k , such that

$$\begin{aligned} \int_{\Omega} [\delta \mathbf{\Pi}_h^{k+1} + \frac{\partial \mathcal{G}_h^k}{\partial \mathbf{F}_h^k} \nabla \delta \mathbf{u}_h^{k+1} + (\delta p_h^{k+1} J_h^k + p_h^k J_h^k \mathbf{F}_h^{k,-\text{T}} : \nabla \delta \mathbf{u}_h^{k+1}) \mathbf{I}] : \boldsymbol{\tau}_h &= \int_{\Omega} \mathcal{R}_{\mathbf{\Pi}}^k : \boldsymbol{\tau}_h, \\ \int_{\Omega} [\delta \mathbf{\Pi}_h^{k+1} \mathbf{F}_h^{k,-\text{T}} - \mathbf{\Pi}_h^k \mathbf{F}_h^{k,-\text{T}} (\nabla \delta \mathbf{u}_h^{k+1})^{\text{T}} \mathbf{F}_h^{k,-\text{T}}] : \nabla \mathbf{v}_h & \\ - \int_{\partial \Omega_R} \eta J \mathbf{F}_h^{k,-\text{T}} (\nabla \delta \mathbf{u}_h^{k+1}) \cdot \mathbf{v}_h + \int_{\partial \Omega_N} p_N \mathbf{F}_h^{k,-\text{T}} (\nabla \delta \mathbf{u}_h^{k+1})^{\text{T}} \mathbf{F}_h^{k,-\text{T}} \mathbf{n} \cdot \mathbf{v}_h &= \int_{\Omega} \mathcal{R}_{\mathbf{u}}^k \cdot \mathbf{v}_h, \\ \int_{\Omega} (J_h^k \mathbf{F}_h^{k,-\text{T}} : \nabla \delta \mathbf{u}_h^{k+1}) q_h + \sum_{e \in \mathcal{E}_h} \int_e \frac{\zeta_{\text{stab}}}{h_e} [\delta p_h^{k+1}]_e [q_h]_e &= \int_{\Omega} \mathcal{R}_p^k q_h, \end{aligned} \quad (3.3.1)$$

$$\forall (\boldsymbol{\tau}_h, \mathbf{v}_h, q_h) \in (\mathbb{H}_h, \mathbf{V}_h, Q_h).$$

Here $\mathcal{R}_{\mathbf{\Pi}}^k, \mathcal{R}_{\mathbf{u}}^k, \mathcal{R}_p^k$ are tensor, vector, and scalar residuals associated with the Newton-Raphson linearisation at the previous step k , and $\mathbf{F}_h^k = \mathbf{I} + \nabla \mathbf{u}_h^k$, $J_h^k = \det \mathbf{F}_h^k$. We then update $(\mathbf{\Pi}_h^{k+1}, \mathbf{u}_h^{k+1}, p_h^{k+1})$ by

$$\mathbf{\Pi}_h^{k+1} = \mathbf{\Pi}_h^k + \delta \mathbf{\Pi}_h^{k+1}, \quad \mathbf{u}_h^{k+1} = \mathbf{u}_h^k + \delta \mathbf{u}_h^{k+1}, \quad p_h^{k+1} = p_h^k + \delta p_h^{k+1}.$$

In order to be able to write (3.3.1) in a more straightforward form, we introduce the following linear maps (which are related to the Gâteaux derivatives of the solution operator):

$$\begin{aligned}\mathcal{L}_1^k : \mathbb{H}_h &\rightarrow \mathbb{H}_h, \tau \mapsto \mathcal{L}_1^k(\tau) = \frac{\partial \mathcal{G}_h^k}{\partial \mathbf{F}_h^k} \tau + (p_h^k J_h^k \mathbf{F}_h^{k,-\mathbf{t}} : \tau) \mathbf{I}, \\ \mathcal{L}_2^k : \mathbb{H}_h &\rightarrow \mathbb{H}_h, \tau \mapsto \mathcal{L}_2^k(\tau) = -\mathbf{\Pi}_h^k \mathbf{F}_h^{k,-\mathbf{t}} \tau^{\mathbf{t}} \mathbf{F}_h^{k,-\mathbf{t}},\end{aligned}$$

and the bilinear forms and linear functionals:

$$\begin{aligned}A_1(\mathbf{\Pi}, \tau) &= \int_{\Omega} \mathbf{\Pi} : \tau, \quad A_2(\mathbf{u}, \mathbf{v}) = \int_{\Omega} \mathcal{L}_2^k(\nabla \mathbf{u}) : \nabla \mathbf{v}, \\ A_3(p, q) &= \sum_{e \in \mathcal{E}_h} \int_e \frac{\zeta_{\text{stab}}}{h_e} \llbracket p \rrbracket_e \llbracket q \rrbracket_e, \quad B_1(\mathbf{u}, \tau) = \int_{\Omega} \mathcal{L}_1^k(\nabla \mathbf{u}) : \tau, \\ \tilde{B}_1(\mathbf{\Pi}, \mathbf{v}) &= \int_{\Omega} \mathbf{\Pi} \mathbf{F}_h^{k,-\mathbf{t}} : \nabla \mathbf{v}, \quad B_2(p, \tau) = \int_{\Omega} J_h^k p \operatorname{tr}(\tau), \\ \tilde{B}_3(\mathbf{u}, q) &= \int_{\Omega} (J_h^k \mathbf{F}_h^{k,-\mathbf{t}} : \nabla \mathbf{u}) q, \quad F_1(\tau) = \int_{\Omega} \mathcal{R}_{\mathbf{\Pi}}^k : \tau, \\ F_2(\mathbf{v}) &= \int_{\Omega} \mathcal{R}_{\mathbf{u}}^k \cdot \mathbf{v}, \quad F_3(q) = \int_{\Omega} \mathcal{R}_p^k q.\end{aligned} \tag{3.3.2}$$

Dropping all iteration indices in (3.3.1) then yields

$$\begin{aligned}A_1(\delta \mathbf{\Pi}_h, \tau_h) + B_1(\delta \mathbf{u}_h, \tau_h) + B_2(\delta p_h, \tau_h) &= F_1(\tau_h) \quad \forall \tau_h \in \mathbb{H}_h, \\ \tilde{B}_1(\delta \mathbf{\Pi}_h, \mathbf{v}_h) + A_2(\delta \mathbf{u}_h, \mathbf{v}_h) &= F_2(\mathbf{v}_h) \quad \forall \mathbf{v}_h \in \mathbf{V}_h, \\ \tilde{B}_3(\delta \mathbf{u}_h, q_h) + A_3(\delta p_h, q_h) &= F_3(q_h) \quad \forall q_h \in Q_h,\end{aligned} \tag{3.3.3}$$

where the linear assembly of (3.3.3) can be written as

$$\mathcal{M} \begin{pmatrix} \mathbf{\Pi}_i \\ \mathbf{u}_i \\ p_i \end{pmatrix} = \begin{bmatrix} \mathcal{A}_1 & \mathcal{B}_1 & \mathcal{B}_2 \\ \tilde{\mathcal{B}}_1 & \mathcal{A}_2 & O \\ O & \tilde{\mathcal{B}}_3 & \mathcal{A}_3 \end{bmatrix} \begin{pmatrix} \mathbf{\Pi}_i \\ \mathbf{u}_i \\ p_i \end{pmatrix} = \begin{pmatrix} \mathcal{F}_1 \\ \mathcal{F}_2 \\ \mathcal{F}_3 \end{pmatrix}. \tag{3.3.4}$$

Here block components of the matrix \mathcal{M} each represents the discretisation of its corresponding linear or bilinear form defined in (3.3.2); $\mathbf{\Pi}_i$, \mathbf{u}_i and p_i are respectively the coefficients of the finite element approximations of the updates $\delta \mathbf{\Pi}_h$, $\delta \mathbf{u}_h$ and δp_h ; \mathcal{F}_1 , \mathcal{F}_2 and \mathcal{F}_3 are respectively columns of F_1 , F_2 and F_3 acting on the finite element basis functions [4].

We remark that this linear system is large-scale and expensive to solve, thus requires the adoption of a robust preconditioner to improve the computational efficiency.

3.4 Accuracy verification of the finite-dimensional approximation

Before moving on to the next stage, it is worth testing the accuracy of our finite element approximation of order 0 and 1.

We consider a test problem on the domain $\Omega = (0, 1)^2$. Given exact solutions for displacement and pressure:

$$\mathbf{u} = 0.1(y^2, y^3)^\top, \quad p = x^4 - y^4,$$

the exact solution of Π can be computed using formula (2.2.10). It can be verified that these solutions satisfy the incompressibility constraint and the governing equations (2.2.13)-(2.2.9)-(2.2.11). The body load \mathbf{b} is manufactured from the exact solutions and (2.2.13). The model parameters for the Holzapfel-Ogden energy are defined as

$$\begin{aligned} a &= 0.496, & b &= 0.041, & a_f &= 0.193, & b_f &= 0.176, & a_s &= 0.123, & b_s &= 0.209, \\ a_{fs} &= 0.162, & b_{fs} &= 0.166, & \mathbf{f}_0 &= (1, 0)^\top, & \mathbf{s}_0 &= (0, -1)^\top, \end{aligned}$$

with the stabilisation parameter being $\zeta_{\text{stab}} = 10^{-2}$. To compute the approximate solutions, we implement a Newton-Raphson method which stops whenever the absolute residual drops below a tolerance of 10^{-8} . At each iteration the discrete version of the linear system (3.3.1) is solved with the sparse direct solver **MUMPS** [13][14]. A uniform mesh refinement is then carried out, on each level we compute errors between the approximated and the exact solutions and record the absolute errors together with the convergence rates. Table 3.4.1 below indicates the optimal error decay for the first- and second-order approximations, where DoF stands for the number of degrees of freedom. It can be verified from the table that the first- and second-order approximations (i.e when $l = 0, 1$) are convergent with order $O(h^{l+1})$. Moreover no locking effect is observed. The locking effect refers to the phenomenon where finite element solutions vanish quickly to zero as certain parameters tend to a specific limit [3]. Linear, bilinear, or trilinear finite elements are known to exhibit the locking effect when applied to nearly incompressible elasticity in displacement-based formulations [36]. The absence of locking in this case is a result of adopting an inf-sup stable discretisation of the three-field formulation [36].

DoF	h	$\ \boldsymbol{\Pi} - \boldsymbol{\Pi}_h\ _{0,\Omega}$	rate	$\ \boldsymbol{u} - \boldsymbol{u}_h\ _{1,\Omega}$	rate	$\ p - p_h\ _{0,\Omega}$	rate
$l = 0$							
51	0.707	0.966	—	0.058	—	0.512	—
179	0.353	0.434	1.154	0.029	0.992	0.213	1.259
675	0.176	0.198	1.133	0.014	1.012	0.093	1.191
2,627	0.088	0.093	1.084	0.007	1.009	0.043	1.115
10,371	0.044	0.045	1.045	0.004	1.005	0.021	1.059
41,219	0.022	0.022	1.022	0.002	1.003	0.010	1.029
$l = 1$							
147	0.707	0.164	—	0.006	—	0.088	—
547	0.353	0.041	2.007	0.001	2.001	0.021	2.074
2,115	0.176	0.010	1.999	3.7e-4	2.082	0.005	2.021
8,323	0.088	0.002	2.001	8.9e-5	2.062	0.001	2.007
33,027	0.044	6.3e-4	2.001	2.2e-5	2.025	3.2e-4	2.004

Table 3.4.1: Approximation errors for Kirchhoff stress, displacement, and pressure, associated with the mixed finite element method using different polynomial degrees $l \in \{0, 1\}$ for Holzapfel-Ogden material laws.

The convergence properties outlined above indicate that the approximation choice is optimal with respect to the expected behaviour according to the interpolation properties on each finite-dimensional space.

Chapter 4

Results without preconditioning

We present the numerical results obtained using direct solvers in this chapter, to verify if our steady formulations produce reasonable physiological response. [45][26].

The truncated ellipsoid is used here as a simplified description for the heart geometry:

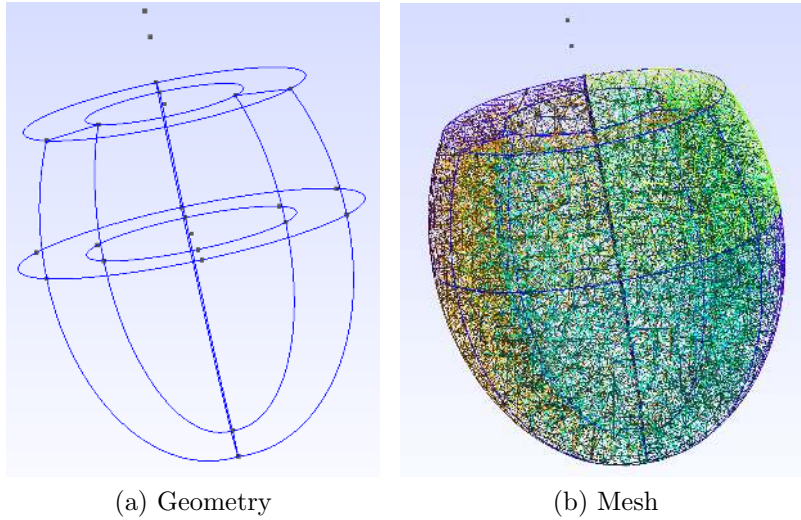


Figure 4.0.1: Geometry and mesh for the ellipsoid, generated using **Gmsh** [31]

Its parametrisation is given by

$$\mathbf{x} = \begin{pmatrix} x \\ y \\ z \end{pmatrix} = \begin{pmatrix} r_s \sin u \cos v \\ r_s \sin u \sin v \\ r_l \cos u \end{pmatrix}, \quad (4.0.1)$$

where r_s refers to the shortest radius and r_l refers to the longest radius of a particular layer of the tissue. The endocardial surface (the inner layer) has $r_s = 1.5$ mm and $r_l = 2.5$ mm, whereas the epicardial surface (the outer tissue) has $r_s = 2.0$ mm and

$r_l = 3.8$ mm. The truncation occurs at the base plane $z = 2.5$ mm. The domain and the 3D mesh generated are demonstrated respectively by (a) and (b) above in figure 4.0.1. Note that this configuration, at its lowest-order discretisation (namely $l = 0$) has only 118143 degrees of freedom - which is not sufficient for many physiologically relevant medical applications.

The material is assumed to have unitary density, with model parameters being specified as follows

$$\begin{aligned} a = 0.496, \quad b = 0.041, \quad a_f = 0.193, \quad b_f = 0.176, \quad a_s = 0.123, \quad b_s = 0.209, \\ a_{fs} = 0.162, \quad b_{fs} = 0.166, \quad \mathbf{f}_0 = (1, 0)^T, \quad \mathbf{s}_0 = (0, -1)^T. \end{aligned}$$

In addition, we take the pressure stabilisation parameter to be $\zeta_{\text{stab}} = 50$, the prescribed boundary pressure $p_N = 0.025 \sin^2(\pi t)$, together with the active tension $T_a = 5 \sin^2(\pi t)$ (where $t \in [0, 1)s$, and $dt = 0.1s$). The fibre directions are visualised as follows:



Figure 4.0.2: Fibre directions on the ellipsoid

We then solve the mechanical system (3.3.4) using the simple damping line search method with full Newton steps. The absolute and the relative convergence tolerance of the line search are both set to be 5.0×10^{-8} . We compute the LU factorisation of the problem, and the linear system associated with each factor is solved by the direct solver MUMPS in PETSc [16][17][18].

The active contraction and inflation of the heart is shown in Figure 4.0.3, where the distribution of pressure (p) is shown over the ellipsoid, with colour red signifying a higher pressure. We observe that the heart first deforms to its most contracted state at $t = 0.5s$ and then recovers its original configuration through inflation.

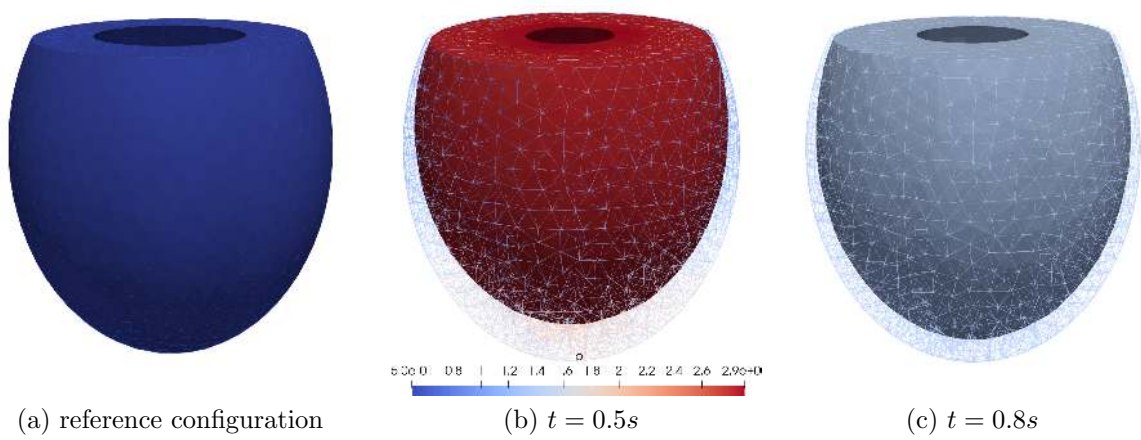


Figure 4.0.3: Contraction and inflation of the ellipsoid

The contraction can be seen more directly by plotting the variation of y-coordinate of the apex over time, the resulting plot 4.0.4 is displayed below, where the apex has contracted from its original position -4.3 to -3.2 .

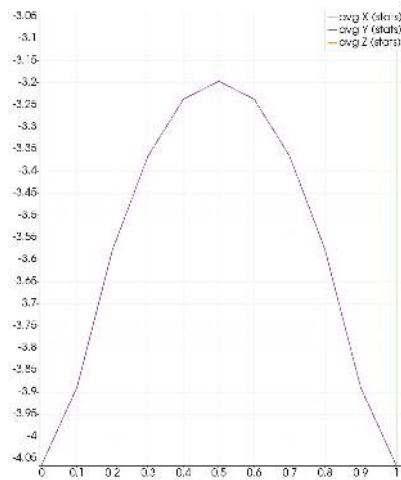


Figure 4.0.4: The y-position of the apex

Note also that there is an effect of wall-thickening during the process of contraction, a cut of the ellipsoid is shown in Figure 4.0.5, and we observe that the wall-thickening is accompanied with an increase in pressure over the ellipsoid.

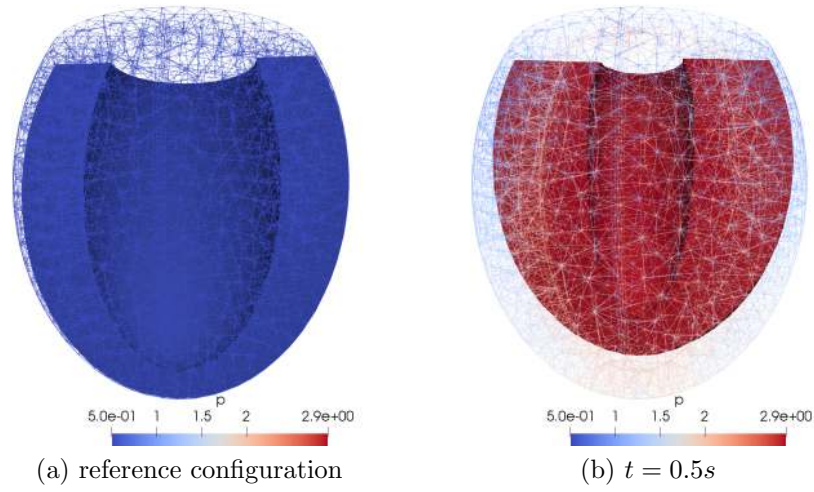


Figure 4.0.5: Wall-thickening of the ellipsoid

Below we also include a colour plot to demonstrate the magnitude of displacement over different parts of the heart, with colour red representing larger magnitude in displacement.

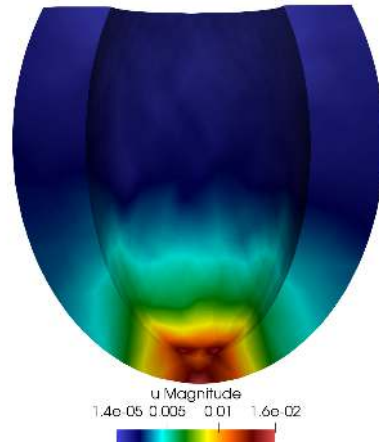


Figure 4.0.6: The displacement plot

As expected, we see that the heart experiences larger displacement in regions near the epicardial apex - a direct consequence of the active contraction.

Therefore we are entitled to conclude from the above observations that, the steady formulations we have used succeeded in producing reassuring qualitative results.

Solving for the system using direct solvers has certain disadvantages, for example the average run time of the code is 12.38 min, leaving us rather a big room for future acceleration. The large-scale and complex nature of the system also restricts

us from taking more than 10^6 degrees of freedom, thus prevents us from taking more sophisticated geometries such as the patient-specific ventricles arising from the real-world medical diagnosis. In addition, since the solutions of the mechanical equations have to be computed at every time step when coupling with the equations of cardiac electrophysiology, the resulting coupled system becomes extremely expensive to solve. The high computational cost rules out any possibility of solving the electromechanical coupling where mesh resolution is vital to capture important physiology phenomenon, such as repolarising patterns.

Chapter 5

Preconditioning

Preconditioning has been and still remains an active area of research in the field of numerical analysis. In this chapter, we first introduce the preconditioning techniques which we will adopt later from a general perspective, then we outline in details how our preconditioner is constructed.

5.1 Overview of preconditioning techniques

The action of preconditioning refers to the transformation of a linear system from its standard form

$$\mathcal{A}u = b, \tag{5.1.1}$$

into another system with more favourable properties for iterative solution [49]. A preconditioner is a matrix \mathcal{P}^{-1} that provides such transformation. The preconditioned system usually takes the form:

$$\mathcal{P}^{-1}\mathcal{A}u = \mathcal{P}^{-1}b. \tag{5.1.2}$$

Through preconditioning, we aim to improve the spectral properties of the matrix \mathcal{A} of the system (5.1.1).

The construction of a high-quality preconditioner is in fact problem-dependent, since the structure of \mathcal{P} relies heavily on knowledge about the matrix \mathcal{A} and exploits to the fullest extent the block structure of \mathcal{A} .

In a broad sense, the convergence rate of the iterative methods applied to (5.1.2) depends on how closely \mathcal{P}^{-1} can approximate the exact inverse of \mathcal{A} . The closer the approximation, the higher the rate of convergence [21].

5.2 Schur complement reduction and the block preconditioner

Schur complement reduction is a common way of reducing linear systems.

For a general non-singular 2×2 block matrix

$$\mathcal{A} = \begin{bmatrix} A & B \\ C & D \end{bmatrix}, \quad (5.2.1)$$

with a non-singular block A , its inverse A^{-1} can be factorised as [39]

$$\mathcal{A}^{-1} = \begin{bmatrix} I & -A^{-1}B \\ 0 & I \end{bmatrix} \begin{bmatrix} A^{-1} & 0 \\ 0 & S^{-1} \end{bmatrix} \begin{bmatrix} I & 0 \\ -CA^{-1} & I \end{bmatrix}. \quad (5.2.2)$$

where

$$S = D - CA^{-1}B \quad (5.2.3)$$

is, by definition, the Schur complement of \mathcal{A} .

One of the possible ways to construct a preconditioner \mathcal{P} , that closely approximates the inverse \mathcal{A}^{-1} , is to make use of the block formula (5.2.2), where the approximation is based on approximations of A^{-1} and S^{-1} . The resulting formula reads

$$\mathcal{A}^{-1} \approx \mathcal{P}^{-1} = \begin{bmatrix} I & -\hat{A}^{-1}B \\ 0 & I \end{bmatrix} \begin{bmatrix} \hat{A}^{-1} & 0 \\ 0 & \hat{S}^{-1} \end{bmatrix} \begin{bmatrix} I & 0 \\ -C\hat{A}^{-1} & I \end{bmatrix}, \quad (5.2.4)$$

where \hat{A}^{-1} and \hat{S}^{-1} are approximations of A^{-1} and S^{-1} respectively. The reason for taking this block factorisation is that, if we see M^{-1} (M being an arbitrary invertible matrix) as the action of solving a linear system $Mx = y$, then the large coupled system (5.1.1) with block structure (5.2.1) reduces to two smaller linear systems involving \hat{A} and \hat{S} , through the operation (5.2.4) [19]. As a result, the availability of fast approximate solvers for linear systems involving A (the top-left block) and S (the Schur complement) are crucial to the performance of the preconditioner defined through (5.2.4).

This choice of preconditioner \mathcal{P} which is given by the block factorisation formula, is called the block preconditioner.

5.3 The augmented Lagrangian preconditioner

In most situations, it is challenging to approximate the Schur complements owing to the dense and indefinite structure they possess [20].

Benzi and Oshanskii proposed, in 2006, an augmented Lagrangian approach which effectively controls the Schur complement for the Oseen problem [20]. The idea, reformulated and supplemented by Fortin and Glowinski in [29] is to introduce an extra term in the variational formulation that does not affect the overall continuous solution, but serves to modify the Schur complement. Eligible candidates are constant multiples of the constraints imposed on each problem, for example the term

$$\gamma \int_{\Omega} \nabla \cdot \mathbf{u} \nabla \cdot \mathbf{v} \, dx$$

is added to the weak form of the Oseen problem, since the particular constraint reads $\nabla \cdot \mathbf{u} = 0$. Here γ is an arbitrary positive constant. Note that this extra term acts as a penalty term for enforcing the constraint, since we are not able to guarantee that the constraint still holds exactly for our discrete solution.

Taking the discrete variation of the new weak formulation (after adding the augmented term) then gives rise to a new block matrix of the linear system:

$$\mathcal{A}_{\gamma} = \begin{bmatrix} A_{\gamma} & B \\ C & D \end{bmatrix}, \quad (5.3.1)$$

where

$$A_{\gamma} = A + \gamma B M_p^{-1} C, \quad (5.3.2)$$

and M_p is the pressure mass matrix defined by

$$(M_p)_{ij} = \int_{\Omega} \rho_i \rho_j \, dx, \quad (5.3.3)$$

with ρ_k being the set of finite element basis functions used for the pressure space [1]. The block factorisation of the inverse of A_{γ} reads

$$\mathcal{A}_{\gamma}^{-1} = \begin{bmatrix} I & -A_{\gamma}^{-1}B \\ 0 & I \end{bmatrix} \begin{bmatrix} A_{\gamma}^{-1} & 0 \\ 0 & S_{\gamma}^{-1} \end{bmatrix} \begin{bmatrix} I & 0 \\ -CA_{\gamma}^{-1} & I \end{bmatrix}, \quad (5.3.4)$$

where the modified Schur complement is given by

$$\begin{aligned} S_{\gamma} &= D - CA_{\gamma}^{-1}B \\ &= D - C(A + \gamma B M_p^{-1} C)^{-1}B, \end{aligned} \quad (5.3.5)$$

and can be simplified by using the Sherman-Morrison-Woodbury inverse formula [15],

$$S_{\gamma} = D + (-(CA^{-1}B)^{-1} - \gamma M_p^{-1})^{-1}. \quad (5.3.6)$$

The augmented Lagrangian approach aids the approximation of the modified Schur complement inverse in a way that by increasing the value of γ we could capture the dominating term of S_γ^{-1} . A good approximation of S_γ^{-1} can thus be obtained simply by discarding the insignificant terms, and setting the approximation \hat{S}_γ^{-1} to have the same dominating behaviour as S_γ^{-1} when $\gamma \rightarrow \infty$. We remark that the approximation developed in this way is problem dependent.

The approximate inverse of \mathcal{A}_γ then reads

$$\mathcal{A}_\gamma^{-1} \approx \mathcal{P}^{-1} = \begin{bmatrix} I & -\hat{A}_\gamma^{-1}B \\ 0 & I \end{bmatrix} \begin{bmatrix} \hat{A}_\gamma^{-1} & 0 \\ 0 & \hat{S}_\gamma^{-1} \end{bmatrix} \begin{bmatrix} I & 0 \\ -C\hat{A}_\gamma^{-1} & I \end{bmatrix}. \quad (5.3.7)$$

From (5.3.7) we remark that, once a good approximation \hat{A}_γ^{-1} of A_γ^{-1} is available, we will be armed with a high-quality block preconditioner.

5.4 Construction of the preconditioner in our particular setting

5.4.1 The field split method

Recall the linear system we introduced at the end of Chapter 3:

$$\mathcal{M} \begin{pmatrix} \Pi_i \\ \mathbf{u}_i \\ p_i \end{pmatrix} = \begin{bmatrix} \mathcal{A}_1 & \mathcal{B}_1 & \mathcal{B}_2 \\ \tilde{\mathcal{B}}_1 & \mathcal{A}_2 & O \\ O & \tilde{\mathcal{B}}_3 & \mathcal{A}_3 \end{bmatrix} \begin{pmatrix} \Pi_i \\ \mathbf{u}_i \\ p_i \end{pmatrix} = \begin{pmatrix} \mathcal{F}_1 \\ \mathcal{F}_2 \\ \mathcal{F}_3 \end{pmatrix}. \quad (5.4.1)$$

In order to fit (5.4.1) into the framework described in Sections 5.1-5.3, it is desirable if \mathcal{M} can be rearranged to become a 2×2 block matrix. We treat (Π, \mathbf{u}) together as one field and p alone remains to be another field. We perform the splitting in this way, such that the pressure block remains at the bottom right corner of the matrix \mathcal{M} , to imitate the structure of \mathcal{M} adopted in [20] and [28], in which robust preconditioners for the Oseen problem have been successfully developed based on the Schur complement reduction method. These works can thus serve as guides for the construction of our preconditioner.

The matrix of the linear system after splitting becomes a 2×2 block matrix, namely

$$\begin{bmatrix} A & B \\ C & D \end{bmatrix} := \mathcal{A}, \quad (5.4.2)$$

where A is a 2×2 block, B is a 2×1 block, C is a 1×2 block, and $D = \mathcal{A}_3$. The

overall linear system reads

$$\mathcal{A} \begin{pmatrix} \mathcal{R}_i \\ p_i \end{pmatrix} = \begin{pmatrix} \kappa \\ \tilde{b} \end{pmatrix}, \quad (5.4.3)$$

where

$$\mathcal{R}_i = \begin{pmatrix} \mathbf{\Pi}_i \\ \mathbf{u}_i \end{pmatrix},$$

$$\kappa = \begin{pmatrix} \mathcal{F}_1 \\ \mathcal{F}_2 \end{pmatrix},$$

and $\tilde{b} = \mathcal{F}_3$.

5.4.2 The augmented term

We recall that the constraint imposed on the cardiac mechanical problem was incorporated into the set of governing equations, namely

$$J - 1 = 0. \quad (5.4.4)$$

So the augmented term being added to the weak form of the variational formulation is the Fréchet derivative of the term

$$\frac{\gamma}{2} \int_{\Omega} (J - 1)^2 \, dx. \quad (5.4.5)$$

We remark that the higher the value we take for γ , the stronger we emphasize on the fulfilment of the constraint. The linear system (5.4.3) after this augmentation then becomes

$$\mathcal{A}_{\gamma} \begin{pmatrix} \mathcal{R}_i \\ p_i \end{pmatrix} = \begin{bmatrix} A_{\gamma} & B \\ C & D \end{bmatrix} \begin{pmatrix} \mathcal{R}_i \\ p_i \end{pmatrix} = \begin{pmatrix} \kappa_{\gamma} \\ \tilde{b} \end{pmatrix}. \quad (5.4.6)$$

5.4.3 The preconditioner

We construct the preconditioner based on the block factorisation formula (5.3.7):

$$\mathcal{P}^{-1} = \begin{bmatrix} I & -\hat{A}_{\gamma}^{-1}B \\ 0 & I \end{bmatrix} \begin{bmatrix} \hat{A}_{\gamma}^{-1} & 0 \\ 0 & \hat{S}_{\gamma}^{-1} \end{bmatrix} \begin{bmatrix} I & 0 \\ -C\hat{A}_{\gamma}^{-1} & I \end{bmatrix}, \quad (5.4.7)$$

where the linear subsystem associated with the top left block \hat{A}_{γ}^{-1} (i.e the approximation to the inverse of A_{γ}^{-1}) is solved directly by the standard LU factorisation. The Schur complement approximation \hat{S}_{γ}^{-1} , on the other hand, requires more deliberate consideration. As mentioned before, finding the approximate inverse \hat{S}_{γ}^{-1} is equivalent to solving a linear system involving \hat{S}_{γ} , so we seek an approximation \hat{S}_{γ} of S_{γ} .

Following from equation (5.3.6), we take the approximation of the modified Schur complement S_γ to be:

$$\begin{aligned} S_\gamma &\approx \tilde{S}_\gamma = D + (-\gamma M_p^{-1})^{-1} \\ &= -\frac{1}{\gamma} M_p + D. \end{aligned} \tag{5.4.8}$$

We remark that D is just the discretisation of the pressure stabilisation term that we have incorporated earlier in Chapter 3, to account for the jump in pressure between adjacent cells. D thus is dependent on ζ_{stab} - the stabilisation parameter.

The processes of solving the linear subsystems associated with \hat{A}_γ^{-1} and \hat{S}_γ^{-1} are known as the inner solves, and the process of solving the overall system after preconditioning is called the outer solve. We try, as the first attempt, to adopt the standard GMRES Krylov iteration (with the maximum number of iterations being one) for the inner solve, and use the standard FGMRES Krylov iteration for the outer solve.

Chapter 6

Results with preconditioning

In this chapter, we present numerical results obtained from solving the preconditioned mechanical system, and provide analysis of the results.

We solve the same cardiac contraction problem which we considered in Chapter 4. The same geometric settings, model parameters, time constraints, and mesh resolution are used here.

According to formula (5.4.8), γ and ζ_{stab} are the two parameters which we can vary when testing the performance of the preconditioner. We demonstrate the performance by showing the evolution of the average number of Krylov iterations (KSP) per Newton step as we refine the mesh, at different values of γ and ζ_{stab} .

Below we show a table of the average KSP per Newton step corresponding to four values of γ and four mesh refinements, ζ_{stab} is taken to be 50 in this case.

# refinements	# degrees of freedom	γ			
		0.1	1	10	100
1	1.2×10^5	12.3	4.15	1.90	1.26
2	3.0×10^5	13.2	4.47	2.01	NF
3	6.7×10^5	15.1	4.86	2.19	NF
4	1.0×10^6	KF	5.21	2.29	NF

Table 6.0.1: Average KSP per Newton iteration at different values of γ with $\zeta_{\text{stab}} = 50$, where KF denotes the convergence failure of the inner Krylov solve, and NF denotes the convergence failure of the outer Newton solve.

We observe a mild decrease in number as γ increases from 0.1 to 100, signifying a decrease in the number of inner solves at each Newton step. As expected, there is also a slight increase in the number of inner solves as we take finer meshes.

The average number of Krylov iterations per Newton step at different values of ζ_{stab} is shown by the table below. We can conclude that varying ζ_{stab} does not affect

the number of inner solves as much as varying γ , in a sense that there is only a slight decrease in iteration number as we increase the value of the stabilisation parameter. Therefore we can conclude that the preconditioner is robust to the pressure stabilisation employed.

# refinements	# degrees of freedom	stabilisation constant (ζ_{stab})		
		0.5	5.0	50.0
1	1.2×10^5	3.04	2.40	1.90
2	3.0×10^5	3.23	2.49	2.01
3	6.7×10^5	3.23	2.64	2.19
4	1.0×10^6	3.21	2.75	2.29

Table 6.0.2: Average KSP per Newton iteration at different values of ζ_{stab} , with $\gamma = 10$

Another feature to capture for the contraction simulation is the convergence in the displacement of the epicardial apex with respect to different mesh refinements, different values of γ , and different values of ζ_{stab} . Given that the epicardial apex is at $(0, -4.3, 0)$ in the undeformed state, its y-coordinate after contraction is plotted against different degrees of freedom (we use the same mesh refinements as those used to produce the Tables 6.0.1 and 6.0.2). We first show the plot for different values of γ .

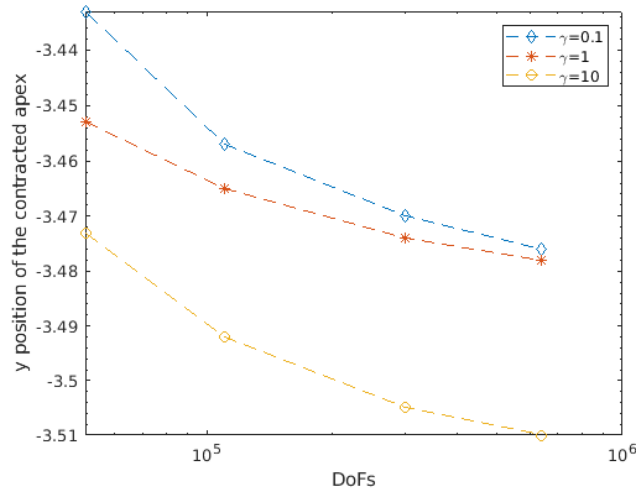


Figure 6.0.1: Convergence plot for the positions of the epicardial apex at different values of γ , when $\zeta_{\text{stab}} = 50$

We observe from Figure 6.0.1 that the apex positions after contraction exhibit some

convergence with respect to mesh refinements for all values of γ . However we notice that when $\gamma = 0.1$ the contracted apex position is getting close to -3.51 (shown by the yellow dashed line), which is lower (but not significantly lower if look from a macroscopic perspective) than the 3.48 obtained from the other two cases. This is because as we increase the value of γ , we are putting more emphasis on the incompressibility constraint which is nonlinear, therefore the mechanical system becomes more nonlinear and gives rise to the slight underestimation in contraction and also the failure in Newton solves.

Varying the stabilisation constant also has an effect on the strength of cardiac contraction. We see from the plot 6.0.2 below that when $\zeta_{\text{stab}} = 0.5$, the apex only experiences a contraction from -4.3 to -3.61 , whereas when $\zeta_{\text{stab}} = 50$, the apex experiences a stronger contraction from -4.3 up to around -3.5 . But again, the final deformed apex positions are not very far apart if viewed from the macroscopic level.

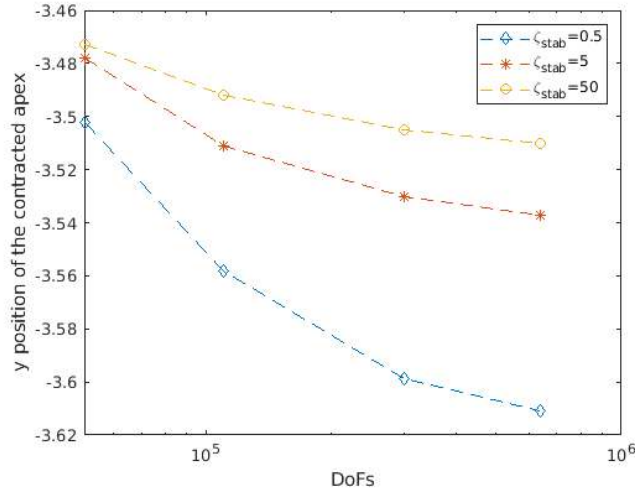


Figure 6.0.2: Convergence plot for the positions of the epicardial apex at different values of ζ_{stab} , when $\gamma = 10$

Solving for the preconditioned system is indeed time-saving, the average run time of the code now, using the same mesh resolution as that of in Chapter 4, is only 2.15 min, almost six times faster than solving the system using direct methods. Another inspiring advantage of adopting the preconditioner is that we are now able to solve the system on a mesh with the number of degrees of freedom being as high as 10^6 . This allows us to construct more realistic domains that better imitate the cardiac structure.

We finalise this section by illustrating the contraction, and more realistically, the twist on a patient-specific left ventricular geometry (segmented from a CT-scan) solved using our preconditioner. We illustrate on subplot (a) of Figure 6.0.3 the mesh adopted for this geometry, and on subplot (b) the fiber generation.

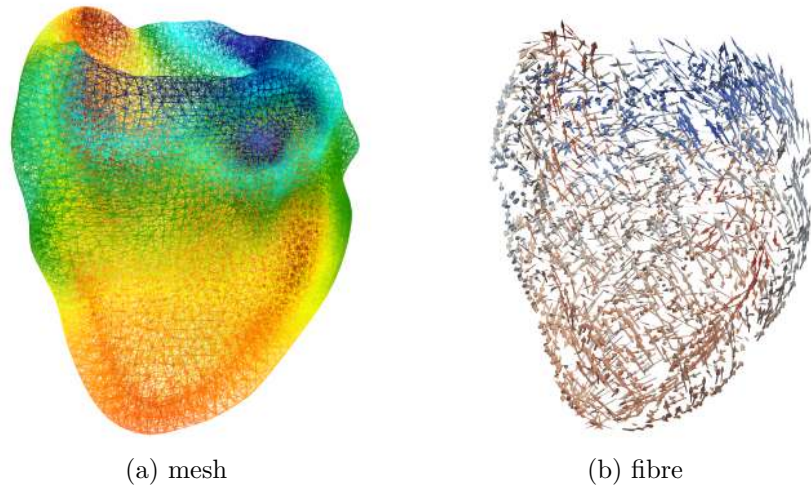


Figure 6.0.3: Mesh and fibre direction on a patient-specific left ventricular geometry

The contraction and the twist of the ventricle are then visualised as follows (the wireframe around the ventricle marks the reference configuration):

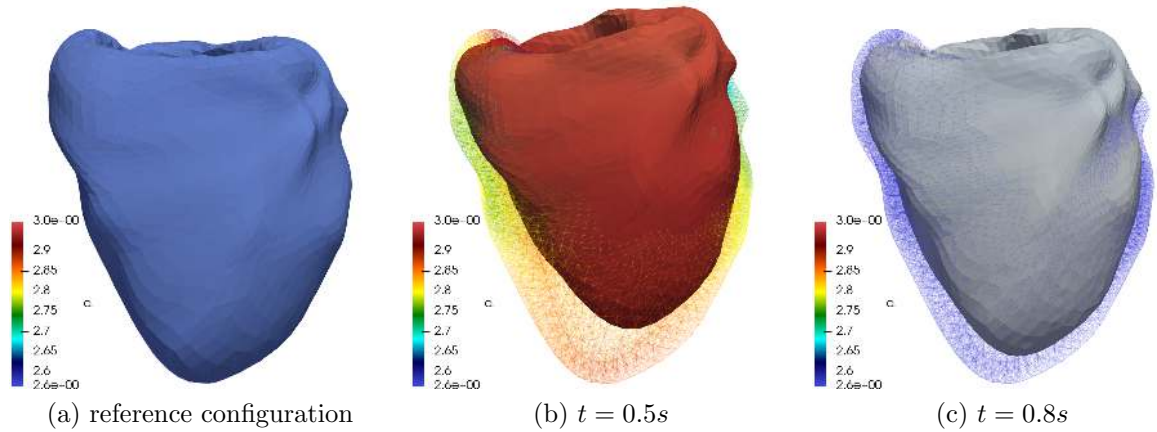


Figure 6.0.4: Contraction, twist, and inflation of the ventricle

The colour map of the displacement is also shown below by Figure 6.0.5, where parts marked by red are displaced the most. This is in accordance with the contraction plot illustrated in Figure 6.0.4, subplot (b).

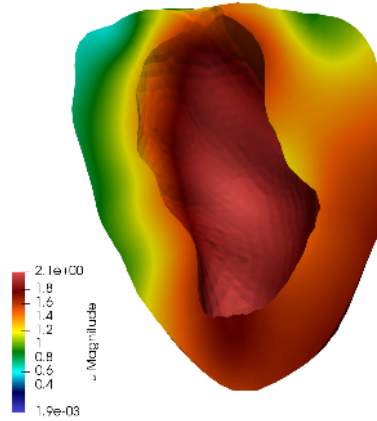


Figure 6.0.5: Colour map of the displacement over different parts of the ventricle

We then make a cut on the ventricle to demonstrate the wall-thickening effect.

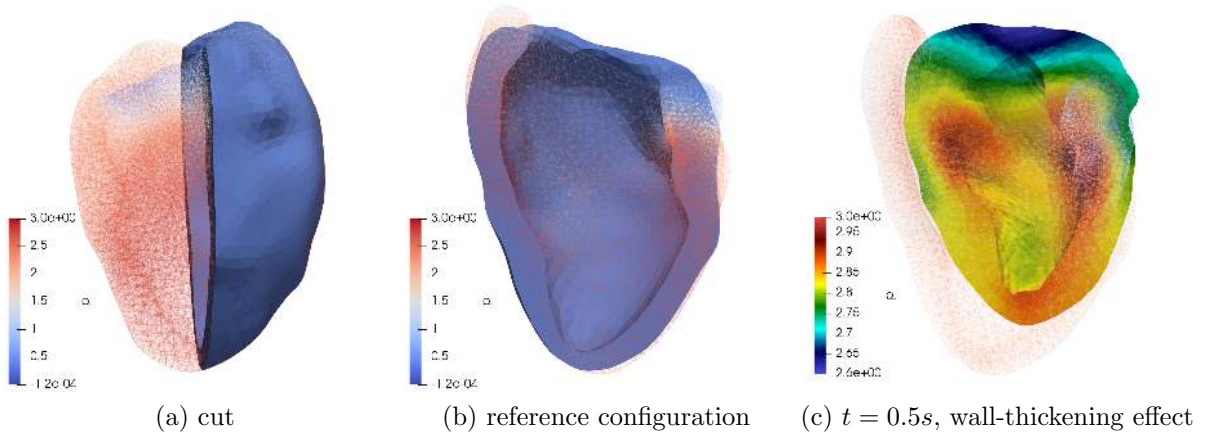


Figure 6.0.6: Wall-thickening effect of the ventricle

We see that at $t = 0.5s$ (also the time when the heart experiences the strongest contraction), the ventricular wall grows to its most considerable thickness, and the inner layer of the endocardium endures the highest pressure.

Note that the number of degrees of freedom being used for this configuration is 1009269. Solving system like this was impossible before incorporating the preconditioner owing to the lack of memory. The adoption of the preconditioner has improved the computational efficiency, reduced the computational cost, thus will greatly aid the future cardiac diagnosis.

Chapter 7

Tests for the preconditioner

It is crucial to validate the preconditioner. We verify the accuracy of our preconditioner by implementing it on two benchmark problems introduced in [37], where quantitative results were proposed in [23].

7.1 Test 1: deflection of a beam

We first consider the deflection of a beam.

The undeformed geometry of the beam is defined by

$$x \in [0, 10], \quad y \in [0, 1], \quad z \in [0, 1] \text{ mm},$$

where the fibre direction is taken to be $f = (0, 0, 1)^T$, and constitutive parameters for the transversely isotropic relations are given by

$$C = 2\text{kPa}, \quad b_f = 8, \quad b_t = 2, \quad b_{fs} = 4.$$

The left face of the beam (i.e the face where $x = 0$) is fixed in all directions, and a pressure of 0.004kPa is applied to the entire bottom face (i.e the face where $z = 0$). The mesh geometry of the beam is generated using **BoxMesh** in **Firedrake** and is shown below

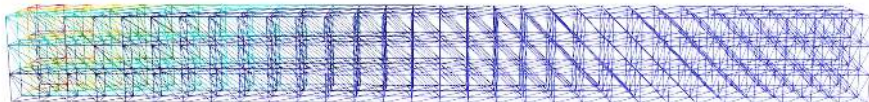


Figure 7.1.1: Mesh of geometry of the beam

The deflection of the beam is visualised as follows (where the wireframe marks the undeformed geometry):

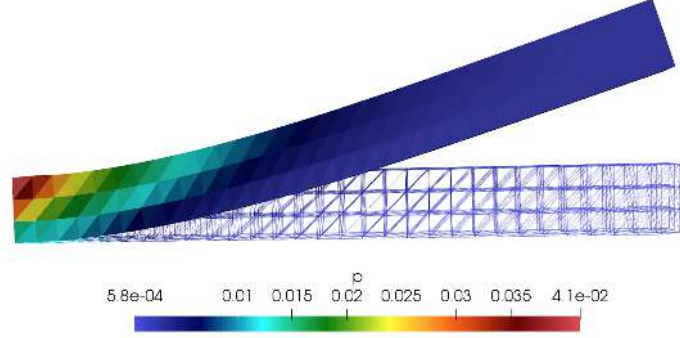


Figure 7.1.2: Deflection of the beam

The side toggle colour legend shows the pressure. We observe that, as expected, the fixed end of the beam is under the highest pressure.

The performance of the preconditioner is again examined by looking at the average number of Krylov iterations per Newton step. Below in table 7.1.1 we illustrate average KSP per Newton iteration at different values of ζ_{stab} and different mesh refinements, with γ being fixed at 10.

# refinements	# degrees of freedom	stabilisation constant (ζ_{stab})		
		0.1	1	10
1	1.8×10^4	3.55	2.95	2.50
2	1.4×10^5	3.86	2.86	2.45
3	4.6×10^5	3.96	2.86	2.73
4	1.4×10^6	4.29	3.14	2.73

Table 7.1.1: Average KSP per Newton iteration at different values of ζ_{stab} , where $\gamma = 10$

We observe only a slight decrease in the number of inner solves as we increase the value of the stabilisation parameter. This allows us to conclude that our preconditioner is robust to the pressure stabilisation.

Varying γ , on the other hand, has a greater effect on the average KSP number. We observe from table 7.1.2 below, the large decrease in average KSP as we increase γ , and the slight increase in average KSP as we refine the mesh. Again, the failure of Newton solver is a direct consequence of the increasing nonlinearity.

# refinements	# degrees of freedom	γ			
		0.1	1	10	100
1	1.2×10^4	16.0	6.21	2.50	1.36
2	1.4×10^5	17.4	6.60	2.45	NF
3	4.6×10^5	18.0	7.20	2.73	NF
4	1.0×10^6	18.4	7.60	2.73	NF

Table 7.1.2: Average KSP per Newton iteration at different values of γ , with $\zeta_{\text{stab}} = 10$, where NF denotes the convergence failure of the outer Newton solve

The z -deflection at the end point of the beam is plotted against different degrees of freedom for different values of ζ_{stab} in Figure 7.2.2. Qualitatively the magnitude of z -deflection is converging as we refine the mesh for all values of ζ_{stab} , and prescribing smaller pressure stabilisation results in smaller deflection magnitude. Quantitatively, it was computed by Campos et al. in [23] that the average deflection was around 4.15mm, which agrees with our computation when taking moderate values for ζ_{stab} .

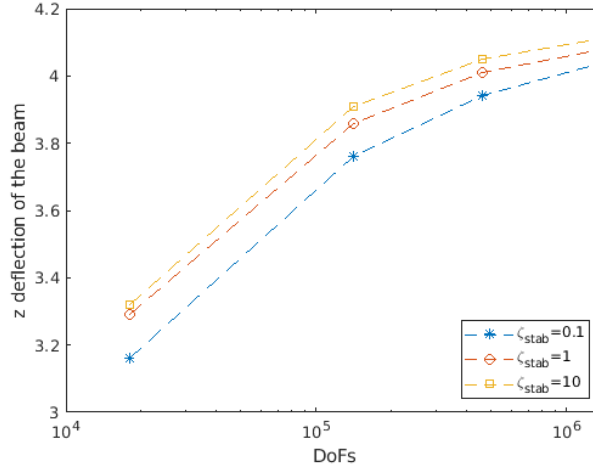


Figure 7.1.3: Convergence plot for z -deflection at the end point of the beam, for different values of ζ_{stab}

The convergence plot for z -deflection of the end point is shown for different values of γ in Figure 7.1.4. Again qualitatively, we observe the convergence in the magnitude of deflection with respect to different mesh resolutions, and quantitatively, the convergence limit agrees with the results established in [23].

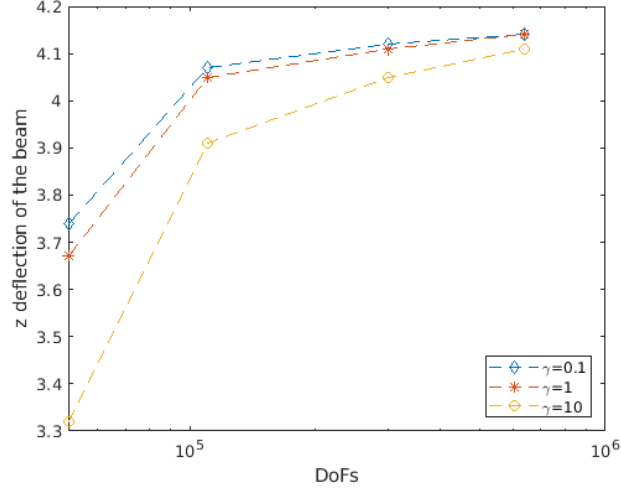
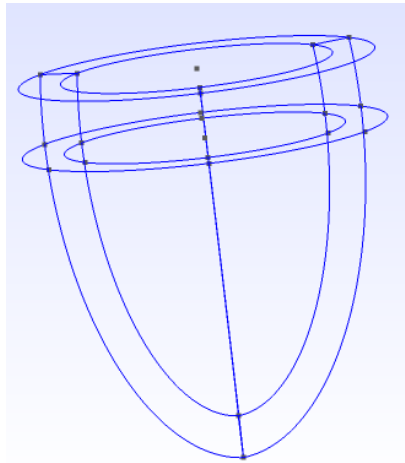


Figure 7.1.4: Convergence plot for z -deflection at the end point of the beam, for different values of γ

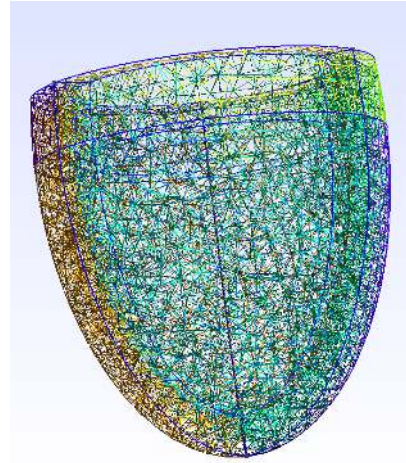
7.2 Test 2: inflation of an ellipsoid

Next we consider the inflation of an ellipsoid.

The geometric construction of such ellipsoid is the same as that being adopted in Chapter 4, but this time with the endocardial surface having $r_s = 7$ mm and $r_l = 17$ mm, and the epicardial surface having $r_s = 10$ mm and $r_l = 20$ mm (where r_s refers to the shortest radius and r_l refers to the longest radius of a particular layer of the tissue).



(a) geometry of the ellipsoid



(b) mesh of the ellipsoid

Figure 7.2.1: Geometry and mesh used for the inflation of the ellipsoid

The truncation occurs at the base plane $z = 5$ mm. The geometry and mesh are shown in Figure 7.2.1. Constitutive parameters of the model are given by

$$C = 10 \text{ kPa}, \quad b_f = b_t = b_{fs} = 1.$$

The base plane ($z = 5$ mm) is assumed to be fixed in all directions and a pressure of 10 kPa is applied to the endocardial surface.

Taking the final time $T_{\text{final}} = 1\text{s}$ with an incrementation of size $0.025s$, $\gamma = 1$, and $\zeta_{\text{stab}} = 5$, we observe the inflation of the ellipsoid (where the wireframe on subplot (b) marks the inflated state):

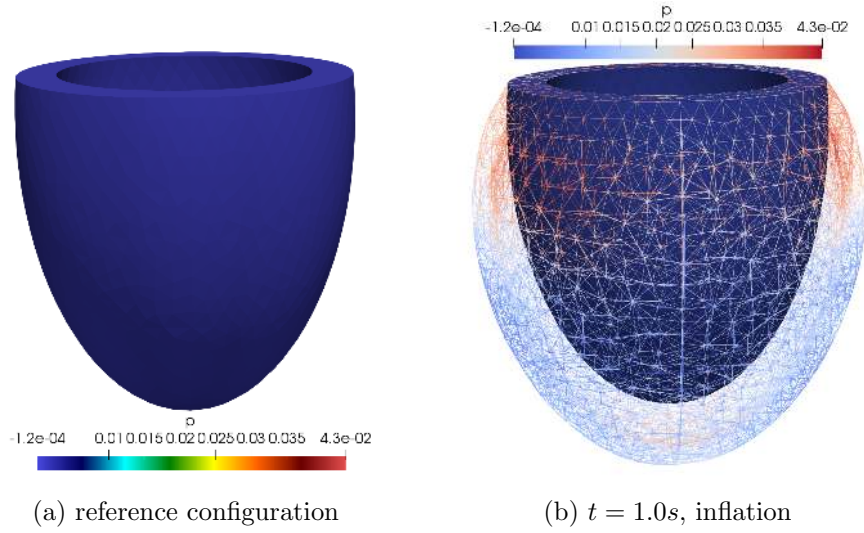


Figure 7.2.2: Inflation of the ellipsoid.

Again, the pressure distribution is shown by the legend, and we note that as the heart inflates, its top part endures higher pressure than its bottom part.

# refinements	# degrees of freedom	stabilisation constant (ζ_{stab})		
		0.5	5	50
1	5.1×10^4	7.26	5.19	4.18
2	1.1×10^5	7.55	5.38	4.25
3	3.0×10^5	8.65	5.75	4.47
4	6.4×10^5	9.02	6.19	4.57

Table 7.2.1: Average KSP per Newton iteration at different values of ζ_{stab} , where $\gamma = 1$

Average KSP per Newton step at different values of ζ_{stab} and different mesh refinements are shown in table 7.2.1 above. We observe the moderate decrease in iteration

number as we take larger stabilisation parameter, and the moderate increase in iteration number as we take finer meshes.

Average KSP per Newton step at different values of γ and different mesh refinements are shown in table 7.2.2 below. We see that increasing γ has a considerable effect on reducing the number of inner solves, and increasing mesh resolution, on the other hand, slightly increases the average KSP.

# refinements	# degrees of freedom	γ		
		0.1	1	10
1	5.1×10^4	14.7	5.19	2.47
2	1.1×10^5	15.4	5.38	2.51
3	3.0×10^5	16.6	5.75	2.58
4	6.4×10^5	17.2	6.19	2.66

Table 7.2.2: Average KSP per Newton iteration at different values of γ , where $\zeta_{\text{stab}}=5$

The convergence plot for the y -inflation of the epicardial apex with respect to different mesh refinements for different values of ζ_{stab} is shown in Figure 7.2.3 below. Given that the apex was at $(0, -23, 0)$ in its original undeformed state, we observe that taking smaller stabilisation parameter results in the convergence to larger inflation magnitude.

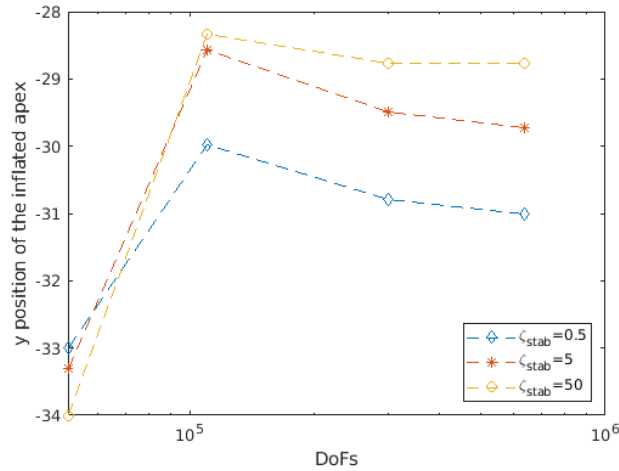


Figure 7.2.3: Convergence plot for apex inflation, at different values of ζ_{stab}

The convergence plot for y -inflation at different values of γ is shown in Figure 7.2.4:

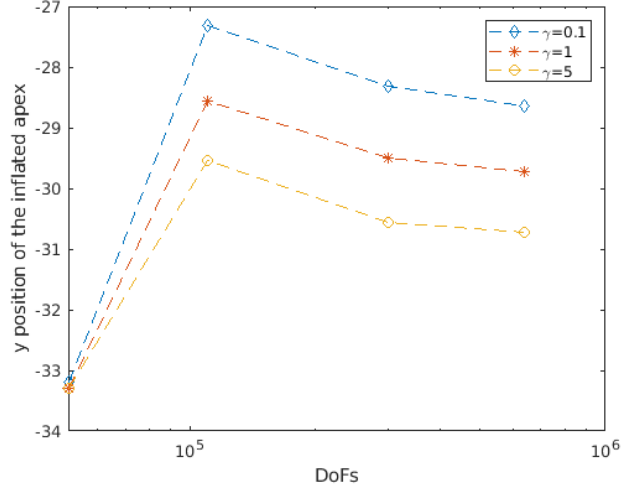


Figure 7.2.4: Convergence plot for apex inflation, at different values of γ

We see that taking larger γ results in the convergence to larger inflation magnitude.

We conclude from both Figure 7.2.3 and Figure 7.2.4 that qualitative convergence of the preconditioner is guaranteed. Quantitatively, it was proposed by Campos et al. in [23] that the y -coordinate of the apex after inflation remains in the range $[-28, -29.5]$ mm, which agrees with our findings when taking $\gamma = 0.1, 1$ and $\zeta_{\text{stab}} = 5, 50$.

Chapter 8

Conclusions and future work

8.1 Conclusions

In this dissertation, we aimed to develop a novel, robust and efficient augmented Lagrangian preconditioner for solving the large-scale cardiac mechanics problem that was recast in a $\boldsymbol{\Pi} - \boldsymbol{u} - p$ three-field formulation.

Serving this purpose, we derived and modified the governing equations to be solved, studied their weak formulations, tested the convergence of the Galerkin discretisation, and discussed the linearisation of the governing equations.

By applying field splitting, the block factorisation formula, and the Schur complement reduction, we succeeded in constructing such a preconditioner, and have validated its performance through a set of benchmark problems.

The preconditioner is efficient in a sense that the inner Krylov iteration is fast, and is robust in a sense that it is stable with respect to the pressure stabilisation term we have incorporated to penalise the pressure jump between adjacent finite element cells. Moreover, when applied to the benchmark problems, reassuring qualitative and quantitative results were obtained for both tests.

8.2 Future work

Recall the block factorisation formula we have used to construct the preconditioner:

$$\mathcal{P}^{-1} = \begin{bmatrix} I & -\hat{A}_\gamma^{-1}B \\ 0 & I \end{bmatrix} \begin{bmatrix} \hat{A}_\gamma^{-1} & 0 \\ 0 & \hat{S}_\gamma^{-1} \end{bmatrix} \begin{bmatrix} I & 0 \\ -C\hat{A}_\gamma^{-1} & I \end{bmatrix}. \quad (8.2.1)$$

We have now a working approximation of the Schur complement, however the linear system involving \hat{A}_γ^{-1} has been solved using the direct LU method. So one of the possible future extensions of this project is to develop a robust approximation of the top left block A_γ .

The computer codes for all the test problems have been implemented using MPI processes with 16 processors, however it is worth testing the numerical results and average run time of the codes implemented with different number of processors.

Moreover it would be helpful to produce a table indicating how the term

$$\int_{\Omega} (J - 1)^2 \, dx$$

varies with different values of γ at different mesh resolutions, since we are expecting to see a better satisfaction of this constraint as γ increases.

Bibliography

- [1] Augmented lagrangian preconditioners for hyperelasticity equations. unpublished. [report, Oxford University, 2019].
- [2] Cardiovascular - cardiac cycle. <https://www.ncbi.nlm.nih.gov/books/NBK459327/>. [Online; accessed 18-Aug-2019].
- [3] Csic centre for mathematical modelling and computer simulation (c-mmcs) - locking phenomena. <http://www.cmmacs.ernet.in/cmmacs/pdf/ch05.pdf>. [Online; accessed 18-Aug-2019].
- [4] Finite Element Notes. Patrick Farrell. [Oxford University 2019].
- [5] Health encyclopedia - right heart catheterization. <https://www.urmc.rochester.edu/encyclopedia/content.aspx?contenttypeid=135&contentid=40>. [Online; accessed 18-Aug-2019].
- [6] Incompressible material. <https://www.sciencedirect.com/topics/engineering/incompressible-material>. [Online; accessed 24-Aug-2019].
- [7] Simulating 3d orthotropic cardiac electromechanics incorporating stress-assisted diffusion. https://www.maths.ox.ac.uk/system/files/media/2018_Propp_A.pdf. [Online; accessed 24-Aug-2019].
- [8] Unit iii : Cardiovascular - cardiac cycle. <http://www.ucc.mun.ca/~dbehm/Cardiovascular.htm>. [Online; accessed 18-Aug-2019].
- [9] Wikipedia - action potential. https://en.wikipedia.org/wiki/Action_potential. [Online; accessed 18-Aug-2019].
- [10] Wikipedia - hyperelastic materials. https://en.wikipedia.org/wiki/Hyperelastic_material. [Online; accessed 24-Aug-2019].

- [11] Wikipedia - orthotropic materials. https://en.wikipedia.org/wiki/Orthotropic_material. [Online; accessed 24-Aug-2019].
- [12] Wikipedia - sobolev spaces. https://en.wikipedia.org/wiki/Sobolev_space. [Online; accessed 27-Aug-2019].
- [13] P. R. Amestoy, I. S. Duff, J. Koster, and J.-Y. L'Excellent. A fully asynchronous multifrontal solver using distributed dynamic scheduling. *SIAM Journal on Matrix Analysis and Applications*, 23(1):15–41, 2001.
- [14] P. R. Amestoy, A. Guermouche, J.-Y. L'Excellent, and S. Pralet. Hybrid scheduling for the parallel solution of linear systems. *Parallel Computing*, 32(2):136–156, 2006.
- [15] Constantin Bacuta. A unified approach for uzawa algorithms. *SIAM Journal on Numerical Analysis*, 44(6):2633–2649, 2006.
- [16] Satish Balay, Shrirang Abhyankar, Mark F. Adams, Jed Brown, Peter Brune, Kris Buschelman, Lisandro Dalcin, Alp Dener, Victor Eijkhout, William D. Gropp, Dmitry Karpeyev, Dinesh Kaushik, Matthew G. Knepley, Dave A. May, Lois Curfman McInnes, Richard Tran Mills, Todd Munson, Karl Rupp, Patrick Sanan, Barry F. Smith, Stefano Zampini, Hong Zhang, and Hong Zhang. PETSc Web page. <https://www.mcs.anl.gov/petsc>, 2019.
- [17] Satish Balay, Shrirang Abhyankar, Mark F. Adams, Jed Brown, Peter Brune, Kris Buschelman, Lisandro Dalcin, Alp Dener, Victor Eijkhout, William D. Gropp, Dmitry Karpeyev, Dinesh Kaushik, Matthew G. Knepley, Dave A. May, Lois Curfman McInnes, Richard Tran Mills, Todd Munson, Karl Rupp, Patrick Sanan, Barry F. Smith, Stefano Zampini, Hong Zhang, and Hong Zhang. PETSc users manual. Technical Report ANL-95/11 - Revision 3.11, Argonne National Laboratory, 2019.
- [18] Satish Balay, William D. Gropp, Lois Curfman McInnes, and Barry F. Smith. Efficient management of parallelism in object oriented numerical software libraries. In E. Arge, A. M. Bruaset, and H. P. Langtangen, editors, *Modern Software Tools in Scientific Computing*, pages 163–202. Birkhäuser Press, 1997.
- [19] Michele Benzi, Gene H Golub, and Jörg Liesen. Numerical solution of saddle point problems. *Acta numerica*, 14:1–137, 2005.

- [20] Michele Benzi and Maxim A Olshanskii. An augmented lagrangian-based approach to the oseen problem. *SIAM Journal on Scientific Computing*, 28(6):2095–2113, 2006.
- [21] Michele Benzi and Miroslav Tuma. A sparse approximate inverse preconditioner for nonsymmetric linear systems. *SIAM Journal on Scientific Computing*, 19(3):968–994, 1998.
- [22] Erik Burman and Miguel A Fernández. Galerkin finite element methods with symmetric pressure stabilization for the transient stokes equations: stability and convergence analysis. *SIAM Journal on Numerical Analysis*, 47(1):409–439, 2008.
- [23] Joventino Oliveira Campos, Rodrigo Weber dos Santos, Joakim Sundnes, and Bernardo Martins Rocha. Preconditioned augmented lagrangian formulation for nearly incompressible cardiac mechanics. *International journal for numerical methods in biomedical engineering*, 34(4):e2948, 2018.
- [24] KS Chavan, Bishnu Prasad Lamichhane, and Barbara I Wohlmuth. Locking-free finite element methods for linear and nonlinear elasticity in 2d and 3d. *Computer Methods in Applied Mechanics and Engineering*, 196(41-44):4075–4086, 2007.
- [25] Francisco Sahli Costabal, Felipe A Concha, Daniel E Hurtado, and Ellen Kuhl. The importance of mechano-electrical feedback and inertia in cardiac electromechanics. *Computer methods in applied mechanics and engineering*, 320:352–368, 2017.
- [26] Lisandro D Dalcin, Rodrigo R Paz, Pablo A Kler, and Alejandro Cosimo. Parallel distributed computing using python. *Advances in Water Resources*, 34(9):1124–1139, 2011.
- [27] F Dorri, PF Niederer, and PP Lunkenheimer. A finite element model of the human left ventricular systole. *Computer methods in biomechanics and biomedical engineering*, 9(5):319–341, 2006.
- [28] Patrick E Farrell, Lawrence Mitchell, and Florian Wechsung. An augmented lagrangian preconditioner for the 3d stationary incompressible navier-stokes equations at high reynolds number. *arXiv preprint arXiv:1810.03315*, 2018.

- [29] Michel Fortin and Roland Glowinski. *Augmented Lagrangian methods: applications to the numerical solution of boundary-value problems*, volume 15. Elsevier, 2000.
- [30] Emilio Garcia-Blanco, Rogelio Ortigosa, Antonio J Gil, Chun Hean Lee, and Javier Bonet. A new computational framework for electro-activation in cardiac mechanics. *Computer Methods in Applied Mechanics and Engineering*, 348:796–845, 2019.
- [31] Christophe Geuzaine and Jean-François Remacle. Gmsh: A 3-d finite element mesh generator with built-in pre-and post-processing facilities. *International journal for numerical methods in engineering*, 79(11):1309–1331, 2009.
- [32] Julius M Guccione, Kevin D Costa, and Andrew D McCulloch. Finite element stress analysis of left ventricular mechanics in the beating dog heart. *Journal of biomechanics*, 28(10):1167–1177, 1995.
- [33] Myrianthi Hadjicharalambous, Jack Lee, Nicolas P Smith, and David A Nordsletten. A displacement-based finite element formulation for incompressible and nearly-incompressible cardiac mechanics. *Computer methods in applied mechanics and engineering*, 274:213–236, 2014.
- [34] A Henderson and A ParaView Guide. A parallel visualization application. *Kitware Inc*, 2007.
- [35] Gerhard A Holzapfel and Ray W Ogden. Constitutive modelling of passive myocardium: a structurally based framework for material characterization. *Philosophical Transactions of the Royal Society A: Mathematical, Physical and Engineering Sciences*, 367(1902):3445–3475, 2009.
- [36] Bishnu P Lamichhane and Ernst P Stephan. A symmetric mixed finite element method for nearly incompressible elasticity based on biorthogonal systems. *Numerical Methods for Partial Differential Equations*, 28(4):1336–1353, 2012.
- [37] Sander Land, Viatcheslav Gurev, Sander Arens, Christoph M Augustin, Lukas Baron, Robert Blake, Chris Bradley, Sebastian Castro, Andrew Crozier, Marco Favino, et al. Verification of cardiac mechanics software: benchmark problems and solutions for testing active and passive material behaviour. *Proceedings of the Royal Society A: Mathematical, Physical and Engineering Sciences*, 471(2184):20150641, 2015.

- [38] Sander Land, Steven A Niederer, and Nicolas P Smith. Efficient computational methods for strongly coupled cardiac electromechanics. *IEEE Transactions on Biomedical Engineering*, 59(5):1219–1228, 2011.
- [39] Malcolm F Murphy, Gene H Golub, and Andrew J Wathen. A note on preconditioning for indefinite linear systems. *SIAM Journal on Scientific Computing*, 21(6):1969–1972, 2000.
- [40] Scan Norburn and David Silvester. Stabilised vs. stable mixed methods for incompressible flow. *Computer methods in applied mechanics and engineering*, 166(1-2):131–141, 1998.
- [41] S Pezzuto, D Ambrosi, and ALFIO Quarteroni. An orthotropic active-strain model for the myocardium mechanics and its numerical approximation. *European Journal of Mechanics-A/Solids*, 48:83–96, 2014.
- [42] S Pezzuto, D Ambrosi, and ALFIO Quarteroni. An orthotropic active-strain model for the myocardium mechanics and its numerical approximation. *European Journal of Mechanics-A/Solids*, 48:83–96, 2014.
- [43] Adrienne Propp, Alessio Gizzi, Francesc Levrero-Florencio, and Ricardo Ruiz-Baier. An orthotropic electro-viscoelastic model for the heart with stress-assisted diffusion. *arXiv preprint arXiv:1905.00262*, 2019.
- [44] Alfio Quarteroni, Toni Lassila, Simone Rossi, and Ricardo Ruiz-Baier. Integrated heartcoupling multiscale and multiphysics models for the simulation of the cardiac function. *Computer Methods in Applied Mechanics and Engineering*, 314:345–407, 2017.
- [45] Florian Rathgeber, David A Ham, Lawrence Mitchell, Michael Lange, Fabio Luporini, Andrew TT McRae, Gheorghe-Teodor Bercea, Graham R Markall, and Paul HJ Kelly. Firedrake: automating the finite element method by composing abstractions. *ACM Transactions on Mathematical Software (TOMS)*, 43(3):24, 2017.
- [46] Ricardo Ruiz-Baier. Primal-mixed formulations for reaction–diffusion systems on deforming domains. *Journal of Computational Physics*, 299:320–338, 2015.

- [47] J Sundnes, S Wall, H Osnes, T Thorvaldsen, and Andrew D McCulloch. Improved discretisation and linearisation of active tension in strongly coupled cardiac electro-mechanics simulations. *Computer methods in biomechanics and biomedical engineering*, 17(6):604–615, 2014.
- [48] TP Usyk, R Mazhari, and AD McCulloch. Effect of laminar orthotropic myofiber architecture on regional stress and strain in the canine left ventricle. *Journal of elasticity and the physical science of solids*, 61(1-3):143–164, 2000.
- [49] Andy J Wathen. Preconditioning. *Acta Numerica*, 24:329–376, 2015.